“There are decades where nothing happens; and there are weeks where decades happen.”
― Vladimir Ilyich Lenin

Long-Term Trends in Optical Airglow Observations in the Canadian High Arctic

By

Dustin Gamblin

B.Sc Physics, University of New Brunswick, 2017

A Thesis Submitted in Partial Fulfillment
of the Requirements for the Degree of

Master of Science

in the Graduate Academic Unit of Physics

Supervisor: William Ward, PhD, Physics

Examining Board: Dennis Tokaryk, PhD, Physics, Chair
Bruce Balcom, PhD, Physics
Adam Dyker, PhD, Chemistry

This thesis is accepted by the
Dean of Graduate Studies

THE UNIVERSITY OF NEW BRUNSWICK

August, 2024

ABSTRACT

The PEARL All-Sky Imager (PASI) is an optical atmospheric imager installed at Eureka, Nunavut, Canada (80N, 86W). PASI is capable of imaging several airglow emissions, though this work is restricted to the sodium doublet (589.3nm), and oxygen green line (557.7nm). Using data from PASI, this thesis develops the following: a systematic calibration routine and the corresponding calibrated images, and a long-term nightglow trend analysis routine including the comparison between seasonal, diurnal, and solar cycle-scale nightglow trends at High (80 degrees) and low (32 degrees) latitudes. This work finds similarities in the seasonal and solar cycle trends, with variations in the sunspot number (SSN) influencing the nightglow brightness on the order of 50%, as well as an SSN dip preceding a brightness dip in winter 2013-2014. This provides further evidence for the circulation of middle atmospheric constituents, along with an estimate for the lag between solar variation, and nightglow variations.

ACKNOWLEDGEMENTS

Thank you to all those who supported me through the last several years including:

Dr. Amy-Rae Gauthier, Dr. William Ward, and my friends and family.

Table of Contents

List of Tables

List of Figures

List of Equations

Chapter 1 – The Airglow

The dynamics and circulation of the atmosphere is a "hot" topic in both the research and public spheres, with most of that interest directed at the lowest reaches of the atmosphere. Known as the troposphere, this is the region where snowstorms, heat waves, and other weather phenomena are experienced. These are dynamical events, but atmospheric movement and evolution are by no means confined to the troposphere. In fact, there is movement throughout the atmosphere, coupling every layer of the atmosphere together, driven by the sun (Zubov et al. 2013). In the mesosphere-lower thermosphere (MLT), the region of interest in this thesis, variations in the sky brightness produced by a phenomenon known as the airglow (or nightglow when confined to night) can be used to infer the tidal movement and seasonal circulation of the atmosphere, as well as the effects of solar radiation. This thesis will study variations in the brightness of the nightglow spanning time scales greater than 2 hours (this excludes gravity waves from consideration) in the Canadian high arctic from the winters of 2009-2018.

Following the brief introduction, this section looks at the historical development of the understanding of airglow, how airglow is produced, and what variations in airglow brightness indicate about the long-term dynamical events occurring in the middle atmosphere of Earth. Chapter 2 will introduce the primary instrument used in the collection of data for this work, the PEARL All-Sky Imager (PASI), and the steps taken to extract calibrated "clean" data from the raw images. Chapter 3 walks through the data preparation and interpretation of the trends present within the dataset and compares the results with

other work done further south. It is in this Chapter where the contribution of this thesis to the field of airglow study is found; long-term observations of airglow variability in the Canadian high-arctic from the ground showing coupling with the solar cycle (despite the high latitude of the observations), providing evidence of the circulation of atomic oxygen in the upper atmosphere. In the final chapter, Chapter 4, the conclusions within this thesis are summarized, and the possible directions for future work can be found.

Earth's Atmosphere

It is customary to separate the atmosphere into several regions based on the physics one hopes to study and understand. In this work we choose to define a region by how the temperature changes with height, the boundaries of which are determined by a reversal of this behaviour (Figure 1). The lowest layer is called the troposphere and is the layer most familiar to us in our everyday existence. Here the density of air is the highest, and the temperature decreases with height at the environmental lapse rate of 6.5 K/km. The troposphere terminates at a region called the tropopause, defined as the transition zone between the troposphere and stratosphere, and where the lapse rate tends towards zero. While the exact height of the tropopause changes based on latitude and weather phenomena, the tropopause is typically found between the heights of 9 km at the poles, and 17 km at the equator.

Occurring just above the tropopause, 25 km in altitude at the equator or 10 km at the poles, the absorption of energy, primarily by ozone in the UV region of the Solar spectrum, causes the temperature of the atmosphere to increase, giving rise to the next layer, the stratosphere. Here very little mixing occurs. This is the altitude where one might want to conduct experiments with weather balloons for example. Crucially, very little of the UV radiation from the sun passes through this layer, which in turn allows life on the surface to flourish.

The Mesosphere begins above the stratosphere, starting at the stratopause, at approximately 50 km, and extends to the coldest part of the atmosphere (mesopause) at ~100 km. The temperature again decreases, as heating from UV absorption decreases (remembering that UV is absorbed more readily in the Stratosphere). The density here is low, and the constituents mixed due to the robust dynamics in this region. As the altitude surpasses ~100 km another transition zone occurs at what is known as the mesopause. The dissociation of molecular oxygen in the region above the mesopause, known as the thermosphere, and the subsequent diffusion of atomic oxygen down into the mesopause, provides the atomic oxygen from which night-time airglow emissions arise. Importantly, night-time airglow, or nightglow, arises from a different chemistry than day-time airglow (dayglow). Because of the supply of atomic oxygen from above, low density, low temperature, and being well mixed, the mesopause region is the ideal location for nightglow (Murtagh et al. 1989), and is thus the region of interest in this thesis.

The next region, known as the thermosphere, is where the temperature again increases, this time due to the absorption of high-energy particles as well as UV. As mentioned earlier, this region is where a significant fraction of the atomic oxygen found in the mesopause region comes from. Through the photo-dissociation of molecular oxygen, atomic oxygen is produced and diffuses downwards into the mesopause/mesosphere.

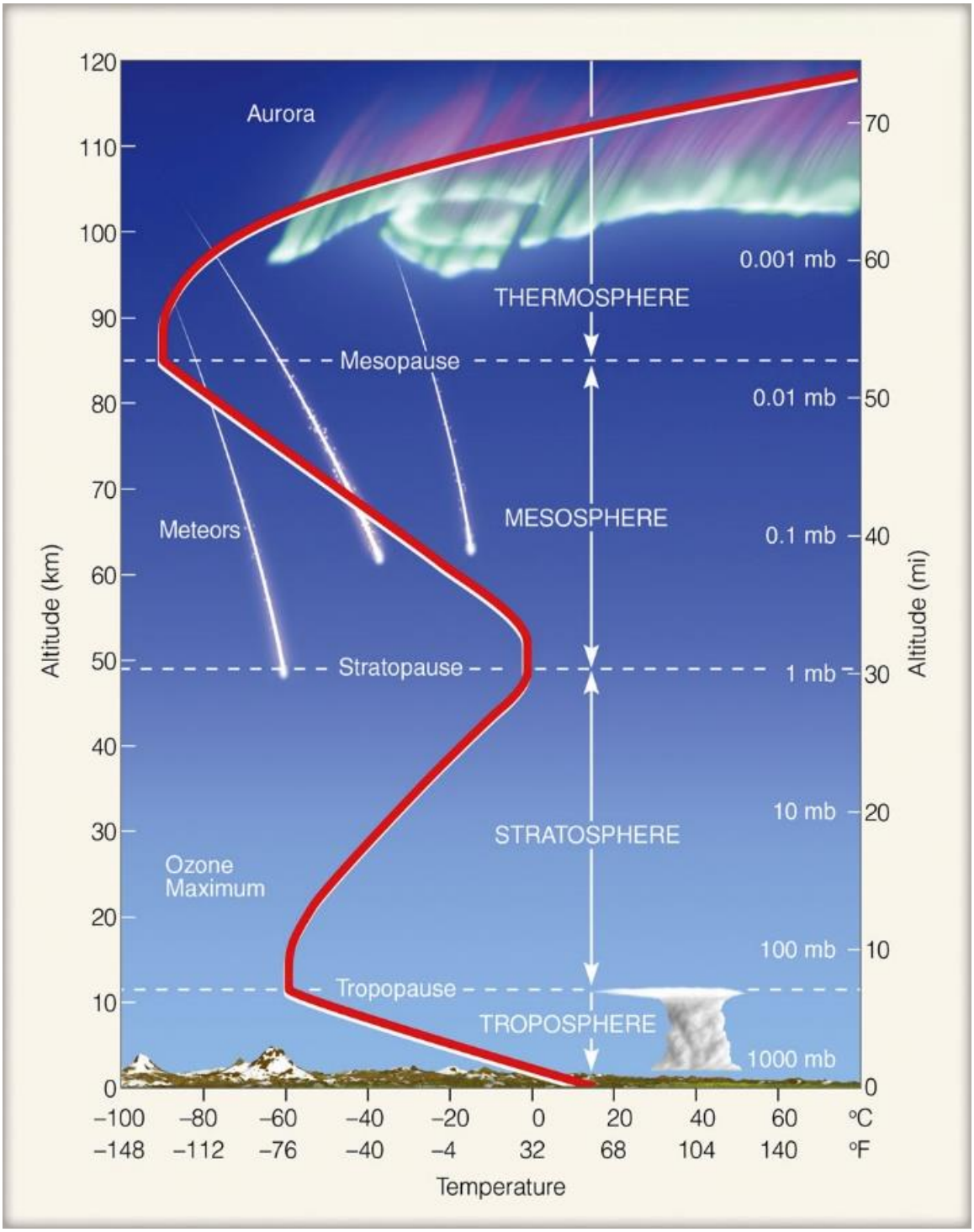

Figure 1: Structure of the atmosphere (Murray 2013)

Airglow Production

The night sky contains many bright objects: stars, planets, the Moon, comets, and faint ones like the nightglow. Throughout the 20th and 21st centuries, rapid improvement in technologies and methodologies have allowed us to observe much more than what is possible with our unaided senses, and thus better understand our natural world. This section introduces the nightglow (airglow being the general term), the topic of this thesis, from the earliest record to the modern understanding.

The earliest record of what may have been airglow comes from the Boshongo's (a Central Bantu tribe in Africa) account of the creation of the world. In their account, the light of the night sky is one of the objects that Bumba, the creator, vomits up into the sky (Silverman, 1970). The earliest measurements of the light that has become known as airglow, were made in the late 1800's and early 1900's where the name "Earth shine" was often used. Though it was also thought early on that this light was in fact just the light of the stars, the light was much greater than could be attributed to the stars alone. Furthermore, the variability in this brightness implied a greater variability in the stars than was likely should they be the sole source of the light of the night sky. Eventually quantitative measurements began to be made in the early 1900's (Russel, 1917), when suitable instrumentation was developed. This led to the suggestion that the light must come from a luminous layer within the atmosphere of Earth, and in the 1920's, measurements within restricted spectral ranges were made by (Rayleigh, 1921). This, at least according to (Silverman, 1970), marks the beginning of modern airglow research.

Much work was undertaken to identify the source of airglow. One “famous” airglow emission is the green line. This emission is both very bright, though still unlikely observable by the unaided eye, and of the same wavelength as the green auroral line. However, unlike the aurora, airglow is not confined to the polar regions and was therefore sometimes known as the “non-polar aurora” (McLennan, 1928), or “light of the night sky”, but from (Elvey, 1950) onward the term airglow is used. Many theorized that green airglow must come from the same or similar region of the atmosphere as the aurora, since it is the same wavelength, and some thought it could be caused by solar influences, like the aurora but without the extreme space weather events associated with aurora. Ultimately the presence of the green line airglow was shown to be decoupled from solar activity, however changes in solar activity have been shown to influence the brightness of airglow emissions at middle latitudes (Das, Pan, and Sinha, 2011).

What, then, produces the light of the night sky? The wavelength of various airglow emissions was isolated by observing the sky in small spectral windows. The green line wavelength was observed to occur in the 550-560 nm region. As it was a green emission a few possible sources were identified. Argon, mercury, and oxygen were all potential candidates, but it wasn’t until (Kaplan, 1931) that a possible mechanism involving atomic oxygen was suggested. Though the accepted mechanism has evolved over time, the green airglow is now known as the atomic oxygen green line.

The atomic oxygen green emission, one of many oxygen emissions, is centred at a wavelength of 557.7nm, the exact same wavelength as the green auroral line. It is also the

brightest of the visible airglow emissions, with brighter emissions occurring in the near infrared. Owing to the abundance of atomic oxygen in the upper atmosphere, this emission is made possible by the photo-dissociation (recalling the abundance of UV radiation in the upper atmosphere) and subsequent recombination of atomic oxygen into molecular oxygen. Though there have been decades of debate about the mechanism, what is known as the "Chapman mechanism" was initially widely accepted as the mechanism bringing about the green emission.

$$O + O + O \rightarrow O_2 + O(^1S)$$

$$O(^1S) \rightarrow O(^3P) + hv$$

However, (Barth and Hildebrandt, 1961) proposed the two-step energy transfer mechanism:

$$O(\,^3P) + O(\,^3P) + M \rightarrow O_2^* + M$$

$$O_2^* + O(\,^3P) \rightarrow O_2 + O(^1S)$$

and the subsequent green line emission.

$$O(\,^1S) \rightarrow O(\,^1D) + hv(\lambda = 557.7nm)$$

Later this mechanism was confirmed by (McDade et al., 1986).

Since there are certain conditions required for this reaction to take place, the possible altitudes for this reaction are limited: the atomic oxygen concentration must be sufficient for three body chemical reactions to take place, but the density must also be low enough that excited atoms are not immediately quenched (Mcdade et al., 1986). It is generally accepted that the green airglow peaks around 96 km in altitude, as shown in Figure 2. Here three rockets were launched (P229H, P230H, P231H) as part of the ETON campaign (McDade et al., 1986), showing the atomic oxygen green line airglow emission altitude measured between 21:27 and 23:13 local time.

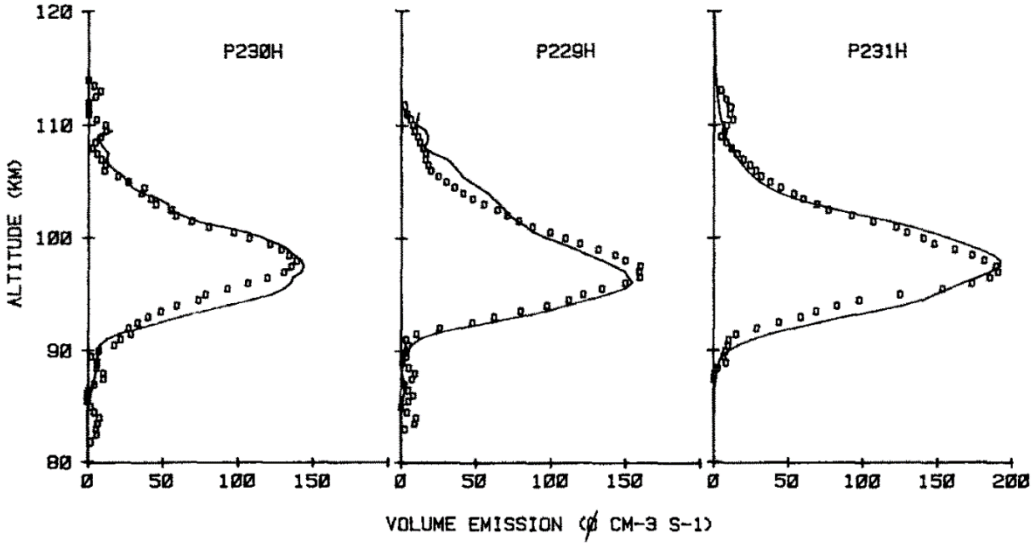

Figure 2: Measured green line emission profiles (open circles) from the ETON rocket mission in photons per cubic centimeter per second (McDade et al., 1986).

The understanding of the sodium doublet (NaD) emission (589.0 nm, 589.6 nm), was developed alongside the development of the understanding of the green line emission. (Chapman, 1939) talks about the source of sodium in the atmosphere as well as the

interesting feature of sunrise/sunset enhancements in the sodium. Early on it was thought that atmospheric sodium might originate from oceans, volcanic dust, meteors, interstellar sodium swept up by earth, or even solar streams of gas. It has since been shown that atmospheric sodium, along with many other atmospheric metals, are due to meteor ablation in the upper atmosphere (~90-100 km altitude) (Plane 1991, 2003). Unsurprisingly this ablation has a seasonality to it (Marsh et al., 2013), whereby more or less metal is deposited into the atmosphere at different times of the year, the pattern of which also depends upon the latitude (Figure 3).

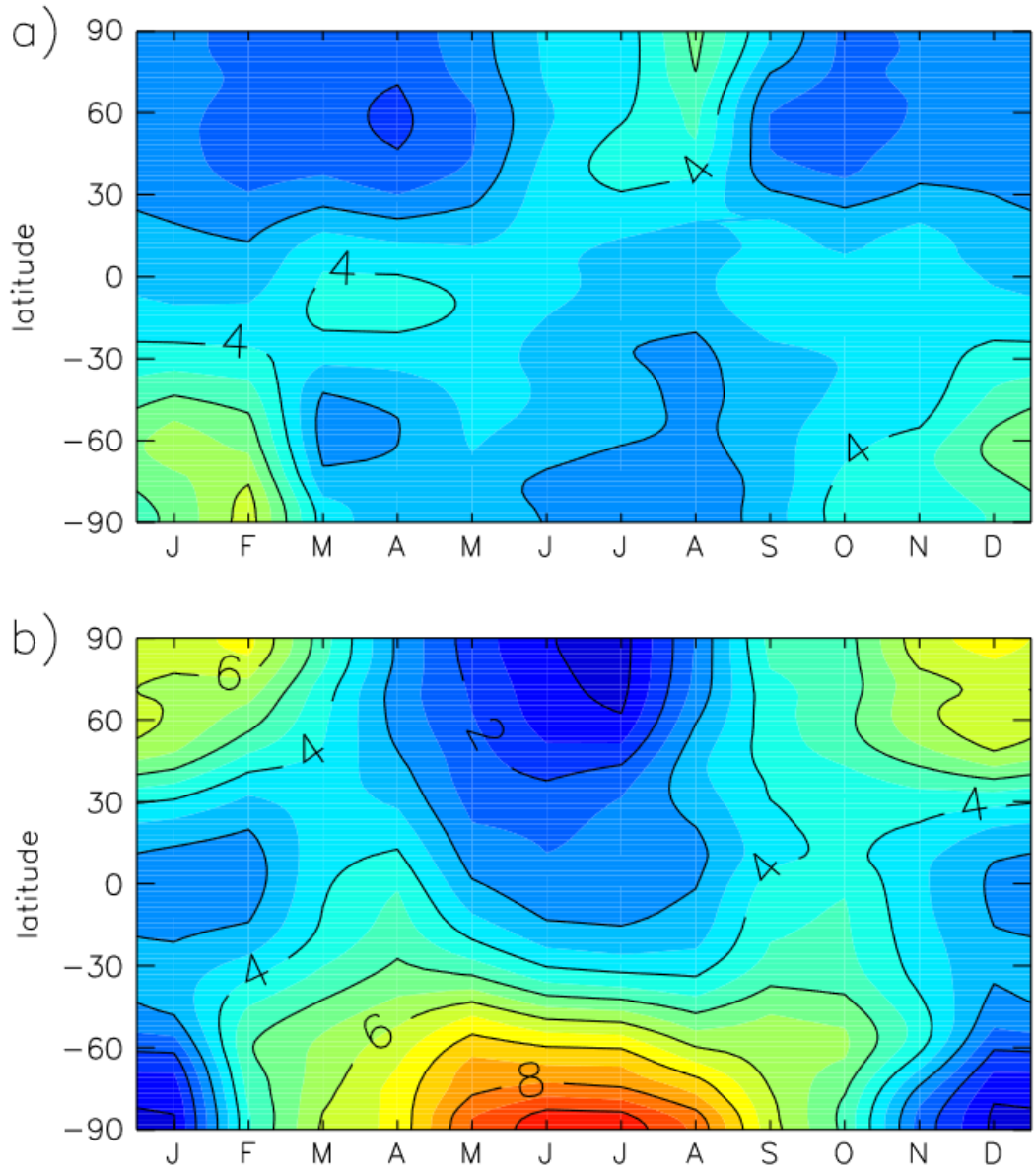

Figure 3: Monthly mean total column density (10^9 atom cm^{-2}) of; (a) Na+, (b) Na, adapted from (Marsh et al., 2013)

A similar variation shows up in the brightness of the sodium emission, shown later in this thesis. In addition, there is a twilight phenomenon which appears in the sodium

emission, where an enhancement in the airglow brightness occurs during both the onset, and outset, of twilight. There are many observations of this phenomena (Barbier and Roach, 1950; Zwick and Shepherd, 1963) however the mechanism is still unclear and, as it occurs during twilight, is outside of the scope of this thesis.

Much like the atomic oxygen green line, the sodium doublet emission involves atomic oxygen from the upper atmosphere, for which the mechanism is suggested to be:

$$NaO + O \rightarrow Na(^2P) + O_2$$

This is known as the Chapman mechanism. However (Silverman, 1970) also states that this method is "not universally accepted" and "additional work… is needed before the mechanism is definitely proven". (Plane et al., 2012; Slanger et al., 2005) have done that additional work, and find the modified Chapman mechanism (Chapman, 1939), to be :

$$Na + O_3 \rightarrow NaO^* + O_2$$

$$NaO^* + O \rightarrow Na\left(^2P_j\right) + O_2 \quad f$$

$$NaO^* + O \rightarrow Na(^2S) + O_2 \quad \textit{(f-1)}$$

f is the branching ratio for the production of excited Na atoms which then fluoresce to generate the sodium doublet emission (Plane et al., 2012). NaD is found at a similar altitude to the green line emission (~90 km) (Clemesha et al., 1993), and shares a similar chemistry.

Thus, these two emissions can be interpreted similarly, and their variations are the topic of this thesis.

Airglow and Atmospheric Changes

The region of the atmosphere of interest for this thesis is known as the MLT (mesosphere-lower thermosphere, or simply the mesopause) and is around 90 km above the surface of the planet. In this region the density is low and decreases with height. This not only allows atmospheric waves to propagate through the layer, but the low density, and thus relatively long duration between atomic/molecular collisions, is the perfect situation to allow for the "forbidden" transitions responsible for much of the airglow to occur. Studying the region of the atmosphere where airglow occurs gives insight into the dynamics of the atmosphere. Perturbations (e.g. upwards and downwards movement) in the airglow layer caused by dynamics like waves and tides appear as periodic changes in the observed brightness of the airglow itself. Unsurprisingly, atmospheric dynamics (e.g., tides, pole-to-pole circulation) permeate the entire atmosphere, propagating around the atmosphere and causing other dynamics. As these dynamical events pass through the MLT, the brightness of the airglow changes in response to the events, acting like a canvas from which atmospheric motions can be inferred. Unlike other observation methods which involve active techniques for atmospheric observations (e.g., meteor radar, requires the production of a radio wave and its reflection, LIDAR requires the generation of a laser beam and its reflection), airglow imaging is a passive technique as airglow is always present in the atmosphere. If there is line of sight from the instrument to observation point, and one is clever enough, the airglow can be measured, and the atmospheric dynamics can be inferred.

Much of the current work in airglow; made possible by ground based, rocket, and satellite observations, involves understanding the latitudinal, vertical, and temporal distribution of various emissions, and using this knowledge to look at dynamics within the atmosphere. This is called using airglow as a tracer. One use of airglow is the investigation of tidal signatures. As a wave moves through the airglow, the atomic oxygen in the atmosphere is moved vertically. This causes a peak in airglow emission intensity in the troughs of the wave and a minimum at the peaks. From here it is possible to measure several wave properties such as the speed, wavelength, and direction, just like any other wave. The mechanism underlying this wave induced variability is nicely summarized in the paper by (Ward, 1999).

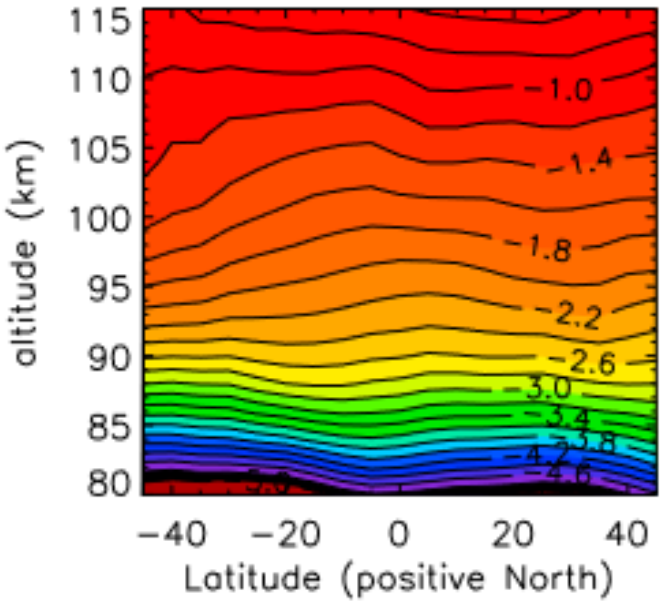

Figure 4: Log of mean atomic oxygen mixing ratios (g kg $^{-1}$) for northern winter (Russell et al., 2005) and local midnight under solstice conditions

Figure 4 shows that atomic oxygen mixing ratio increases with altitude. The volume emission rate of airglow increases with mixing ratio, density, and temperature (Ward,

1999). If a region of air (we'll call it an air parcel) is moved downwards by a passing wave, the higher mixing ratio of the air parcel now in a region of greater density and temperature, will have a greater volume emission rate. Thus, as mentioned before, the troughs of a wave show up bright in the airglow layer. The same is true for the sodium emission, albeit at a slightly lower height (92 km, (Clemesha et al., 2005)). It then stands to reason that if a region of the atmosphere has an increase in atomic oxygen compared to the average, the brightness of the green and sodium airglows increases. In addition, for sodium airglow, an increase in atmospheric sodium corresponds to an increase in sodium airglow brightness. In summary, knowing how atmospheric vertical motions, and changes in local chemistry, affect the brightness of airglow, makes it possible to better interpret the source of these changes.

In this thesis there are three variations considered. Diurnal variations, which are due to the vertical motions associated with atmospheric tides (Ward, 1999). Seasonal or normal variations over the course of a year, associated with the movement of reactants from other parts of the planet (Fukuyama, 1977)(the data sets used are for winter/night time airglow, more on this later). And changes in the average brightness from year to year, indicative that a change in solar activity may be to blame (Rosenberg and Zimmerman, 1966).

Motivation For This Thesis

Like any atmospheric measurement, having data sets spanning all of time over the entire globe is the ideal situation. The closer data sets come to this goal the better the understanding, prediction of atmospheric norms, and forecasting can be. In the case of airglow, independent quantitative measurements have been made since the early 1900's (Rayleigh, 1922). As the century progressed and space flight became possible, airglow measurements over the middle latitudes became possible with satellites (Shepherd et al., 1993) and, when combined with land-based observations (Dandekar and Silverman, n.d.; Hapgood, 1982) and weather balloons (Donahue et al., 1968), a complete picture of atmospheric airglow emission seemed within reach. Unfortunately, satellites are unable to observe the same location with a very high cadence, making short term variations difficult to observe. Singular ground-based instruments are limited by their location, and rockets and weather balloons are short lived experiments. However, these approaches clearly support each other. So where then does this thesis come in? Satellites can cover some of the polar regions, but ground-based observations are difficult to make by virtue of the remoteness of the Arctic, and Antarctica. Thus, observations have been sparse, or nonexistent, in these regions making global understanding of atmospheric circulation difficult. However, in 2007 an optical instrument named PASI (PEARL All-Sky Imager) capable of measuring airglow was installed in the Canadian high Arctic at 80°N 86.4°W.

With the continued study of airglow, long term trends can be established and changes in MLT chemistry can be documented. This will help us better understand the effects of climate change, greater CO_2 levels (Huang, 2018; Ward et al., 2021), and a warming planet, on the dynamics and circulation patterns in the atmosphere. How then can we apply what we know of airglow to learn more about airglow, and the atmosphere as a whole? The answer is time scales. We know that gravity waves exist at certain timescales, while pole to pole circulation (downward advection of atomic oxygen), tides, day-night cycle, as well as seasonal activities all occur and will affect the airglow differently. This thesis concerns phenomena which occur at timescales larger than several hours and cause a modulation in the brightness of the airglow. These are summarized in Table 1.

Table 1: Phenomena as they relate to time scales in this thesis

Phenomenon	Time Scale	Part of this Thesis?
Gravity Waves	< 2 hours	No
Tides	Diurnal	Yes
Seasonal Circulation	365 days	Yes
Long Term Solar Effects	11^+ Years	Yes

Data from the instrument known as PASI (PEARL All Sky Imager), is calibrated including steps to ensure high data quality, and compared to variations in other nearby instruments exemplifying the ability to use multiple datasets from these co-located instruments in future studies. This new data set is used to examine trends in the high Arctic

airglow over ~10 years and compared to trends that are typical of more southerly datasets. Nightly, yearly, and long-term variability of the sodium airglow, and the atomic oxygen green line is examined, ensuring only data collected during polar night is incorporated.

This brings us to the realm of current research. The current understanding of airglow provides a foundation for the study of the mesosphere-lower thermosphere (MLT) by observing changes in airglow brightness, Doppler shifts in airglow emission wavelengths, and with molecular emissions, temperature changes are also observable. Each one of these occur at many time scales, and thus give many different varieties of information.

Chapter 2 – PASI Calibration

Nearly all the data present in this thesis originates from PASI (the PEARL All-Sky Imager) in Eureka, Nunavut. A large portion of the work in this thesis is dedicated to ensuring the data from PASI is of consistent quality and can be used for comparisons and studies with other instruments at the same observatory. Ground based instrumentation, such as that used in this thesis, is a relatively inexpensive option for observing the atmosphere. In the case of satellite instrumentation, one must be certain that all aspects of the instrument are in place and operational before launch, after which no physical interventions are possible, and only remote adjustments are possible. For ground-based instrumentation it is possible to simply walk up to the instrument and ensure its proper function as well as modify any aspect deemed necessary. That is, unless that instrument exists in one of the most remote regions of the planet: the Canadian high Arctic. In this section PASI is introduced. The difficulties associated with operating such an instrument in a remote location, the geophysical "noise" associated with ground-based observations, and the strategies employed to overcome such difficulties are described.

Table 2: PASI Filters and Emissions

Filterwheel Position	Filter Wavelength(s) Transmitted (nm)	Emission Observed	Altitude of the Emission (km)	Integration Time (s)
1*	All	All	-	
2	589.3	Sodium	90	
3	572.5	Background	-	
4	720-910 (865 notch)	Hydroxyl Meinel Bands	87	
5	427.8	N^{+}_{2}	-	
6	557.7	OI Green Line	96	
7	630.0	OI Red Line	250	
8*	None	None	-	

*These filterwheel positions have since been replaced with filters capable of imaging day-time airglow (dayglow), and a collar was placed in 2017 to limit stray light from entering the camera

The data from PASI comes in the form of images. The number of photons collected per exposure time is reported and stored in the png format. While it is true that a time stamped series of images and the associated wavelength can be used to infer much about the dynamics of the sky, to measure the proper brightness, and the variation of said brightness, a full calibration must be done. A list of the filters on PASI can be found in Table 2. For the emissions with a proper background channel (sodium and atomic oxygen

green line) this means the final output will be in units of Rayleighs (1R = 10^{10} photons per square metre per column per second). For nitrogen, hydroxyl, and atomic oxygen red line, the output is in counts per second. Included in the calibration are the preliminary data "cleaning" steps. Stars and the background are removed, cloudy days identified, optical depth is estimated, and various geometric corrections are applied. In this chapter, these corrections are introduced and described.

All-Sky Imager

Like other All-Sky Imagers, PASI (Figure 5) is a conceptually simple instrument, consisting of a cooled CCD detector of scientific quality with output resolutions up to 1024x1024 pixels, a filter wheel with up to 8 specially chosen filters, and a fish-eye lens. This set up provides images (Figure 6) of the entire horizon-to-horizon night sky at the wavelengths of common airglow emissions (Table 2) for the entirety of polar night with a high signal to noise ratio. A full description of PASI can be found in the Master's thesis of Dragan Veselinovic (Veselinovic, 2008).

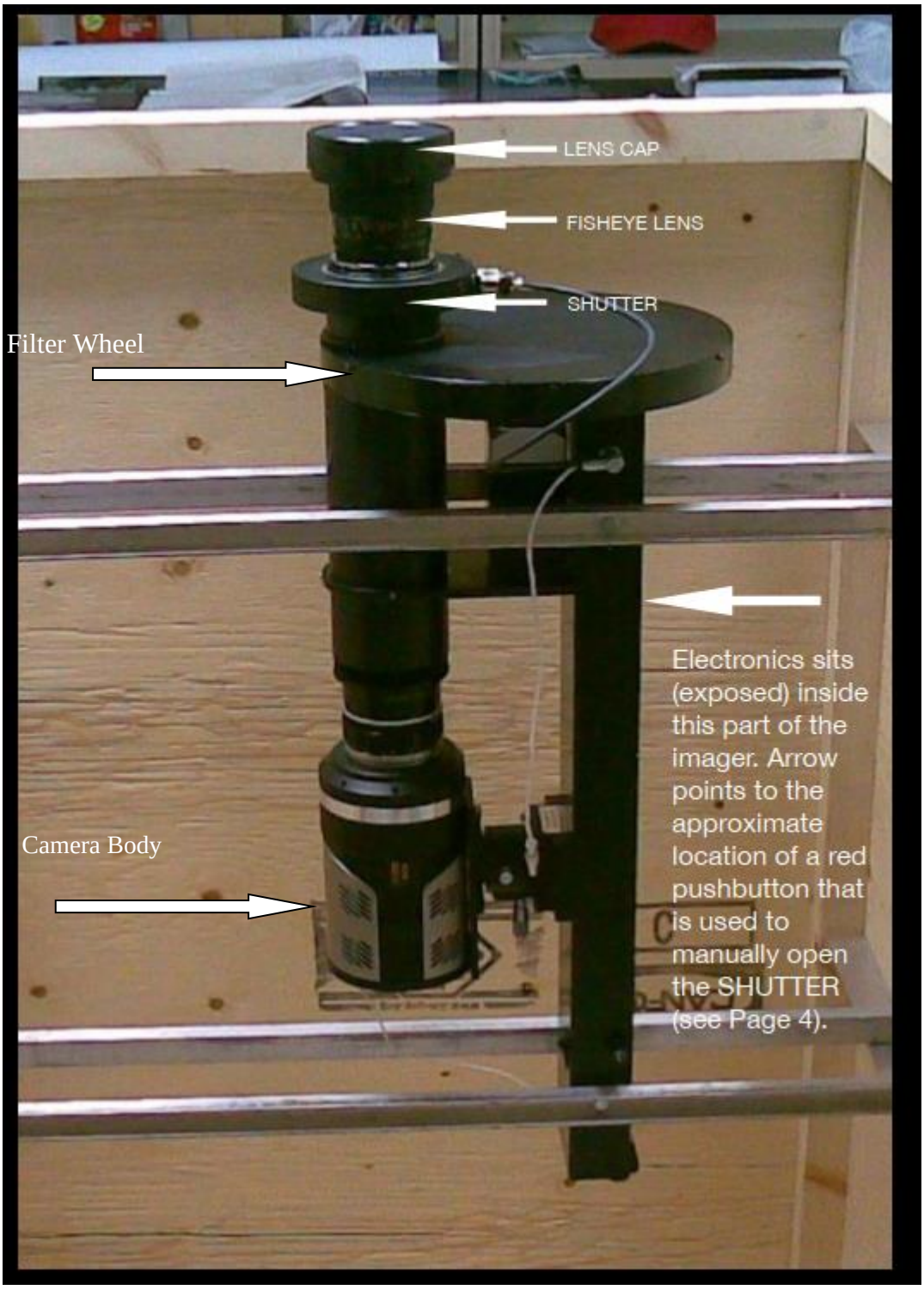

Figure 5: Profile of PASI

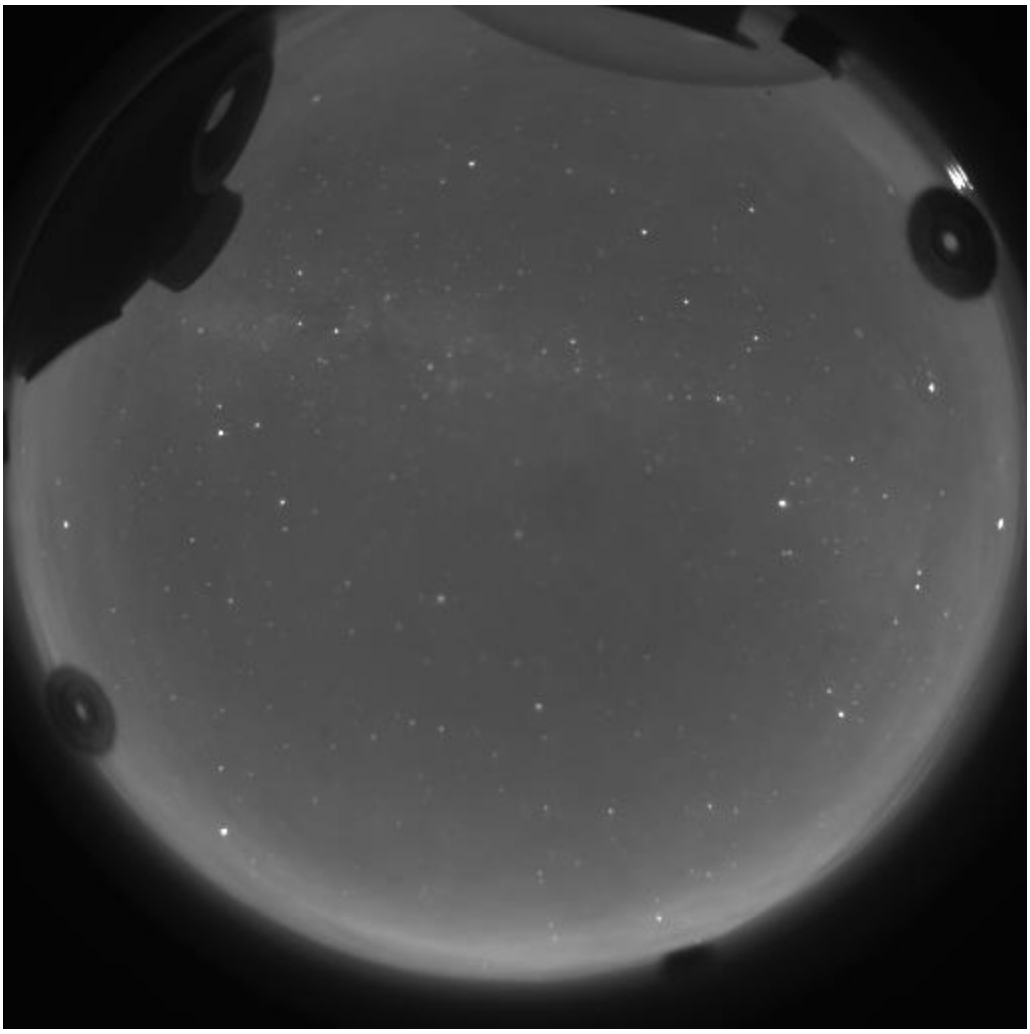

Figure 6: Uncorrected image from PASI showing the sky above Eureka

Figure 7: Location of PASI. Retrieved from danweaver.ca

Locating an optical instrument at such a high latitude (80.06° N, Figure 7) comes with both unique benefits and challenges. First and foremost, PASI must be operated remotely as the only option for accessing PEARL and Eureka is through a chartered flight. It is also very cold in the winter, and care must be taken to ensure the field of view remains free of snow and ice, meaning someone must be present to ensure proper operation. At the PEARL site in Eureka (Figure 7) a CANDAC (Canadian Network for the Detection of Atmospheric Change) staff member provides support (funding dependant) not only for PASI, but a large array of atmospheric instruments, a list of which is available at the following URL: https://www.pearl-candac.ca/website/. This high-latitude position makes it possible to observe the night sky for nearly 5 months, uninterrupted. As the sun sits below the horizon from late October until late February (Figure 8), this provides a unique opportunity to continually observe airglow, and thus atmospheric motions.

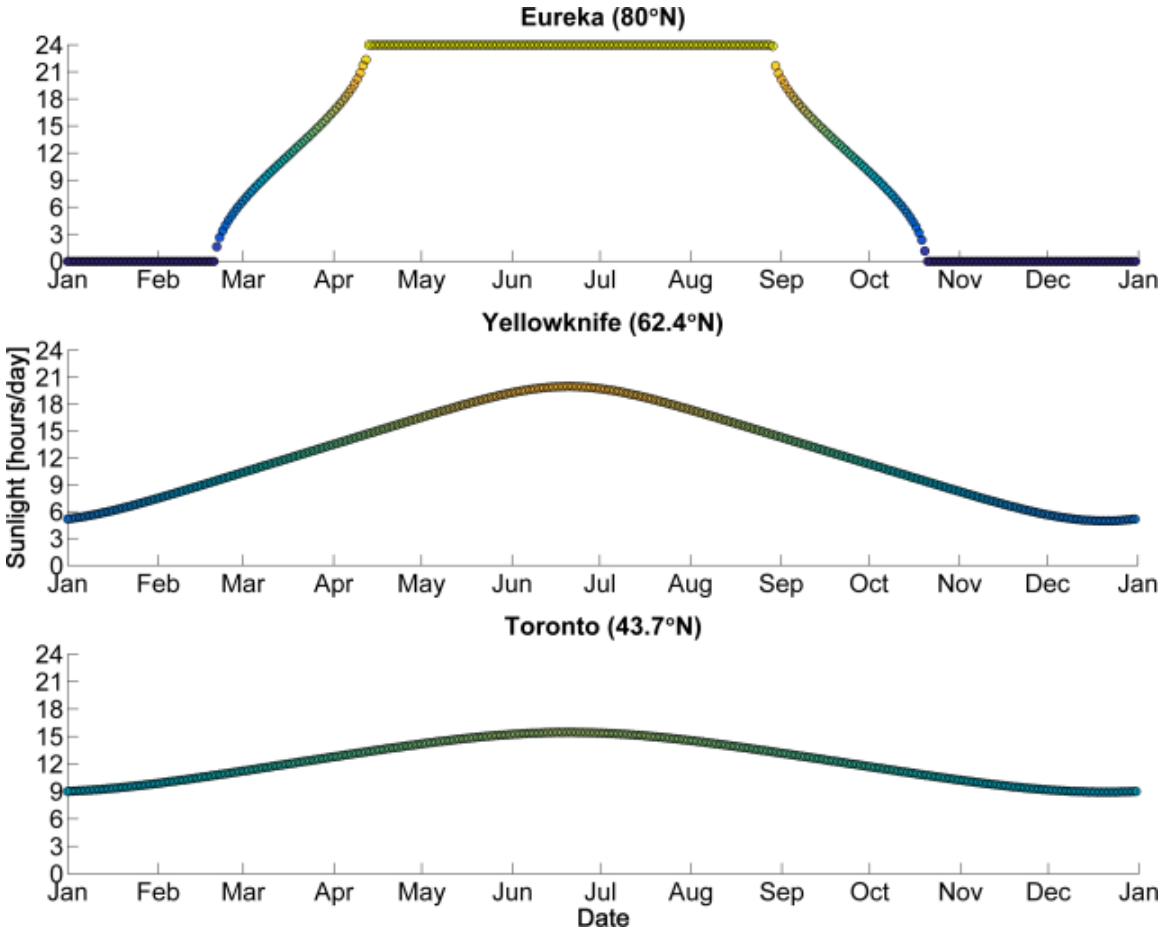

Figure 8: Sunlight hours for various latitudes (Weaver 2016)

The images from PASI are stored in a PNG format, 16-bit unsigned integer. This means only positive values are present, and the maximum value is 65535 counts per-pixel, the saturation point. Finally, the images are temporarily stored locally at PEARL on a laptop before being uploaded to the CANDAC servers down south, and eventually downloaded to the computers here at UNB, where the images undergo the calibration process.

Data Calibration

To extract the highest quality data from PASI, it is necessary that various instrument, atmospheric, and “scene” elements are either corrected for, or removed entirely. These include the presence of stars, correcting for filter characteristics, locating instrument zenith, and correcting for signal attenuation and geometric enhancement. The following sections will introduce and justify the calibration procedures in the order in which they are applied to raw images. To ensure the desired data is provided, the data is calibrated in the order of steps shown in Figure 9. In addition, the images must be sorted such that the appropriate background image is used. The code that has been developed is available upon request, however for the sake of brevity only the steps taken that change the images themselves will be presented here.

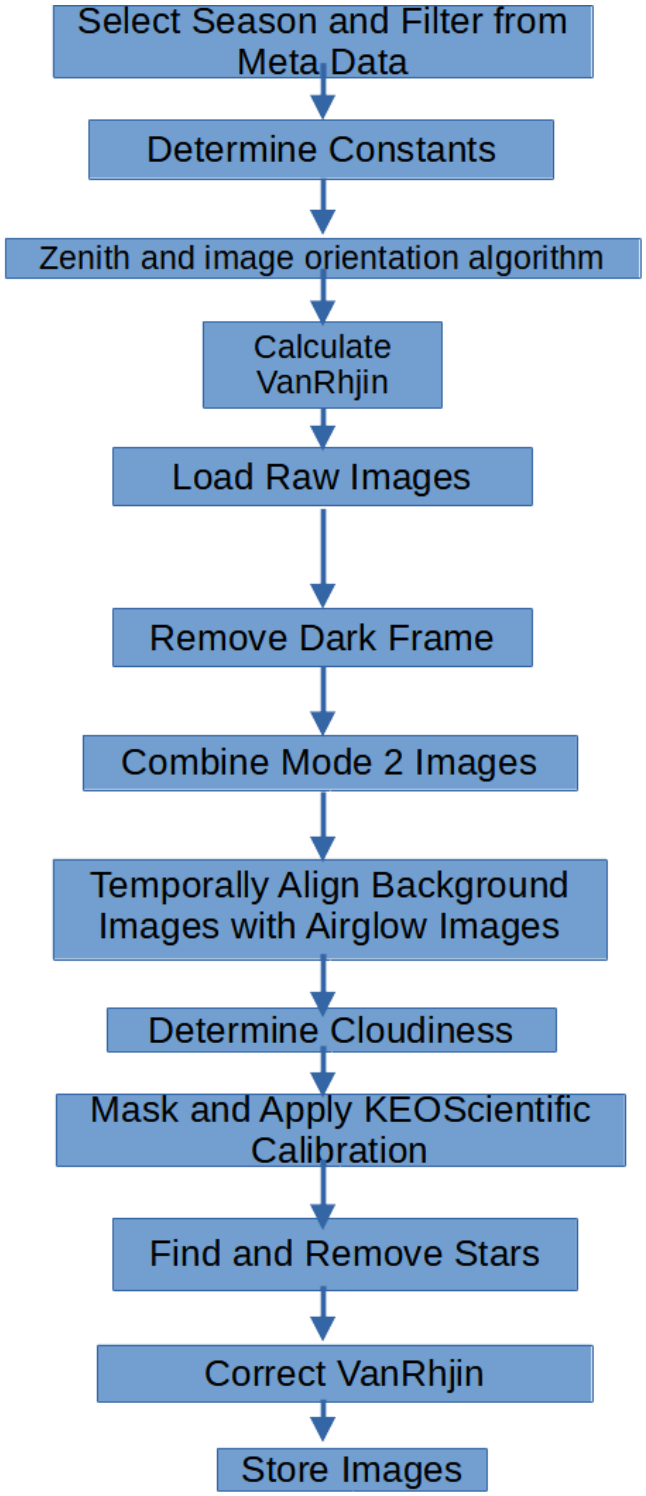

Figure 9: Image correction flowchart

Image Metadata and Instrument Orientation

The first step in the calibration process involves loading the images into memory based on the identifying meta-data. The date, time, airglow emission, and operation mode, are all readable from the image name (Table 3). This metadata indicates which constants should be used for the data set (like height of emitting layer, and exposure time for the chosen filter).

Table 3: Image naming convention

ASI_yyyy_mm_dd_HH_MM_SS_fw_pos_x _mode_n.png	
ASI	Identifies the images as being collected by PASI
yyyy_mm_dd	The year, month, and day of the image acquisition
HH_MM_SS	The hour, minute, and seconds of acquisition, at time of saving
fw_pos_x	Indicates the filter being used for the image (x = [1,8])
mode_n	Indicates the exposure mode, only applicable for data after 2014, indicates an exposure of 5 (mode 2) or 30 (45 for hydroxyl) seconds
.png	The images are saved as a png file

The calibration process will determine the orientation of the image relative to the surface of the Earth. The main result desired for the work in this thesis is the location of zenith, however the direction of North-South is computed, and would be required for any work that involves determining the propagation direction of airglow features.

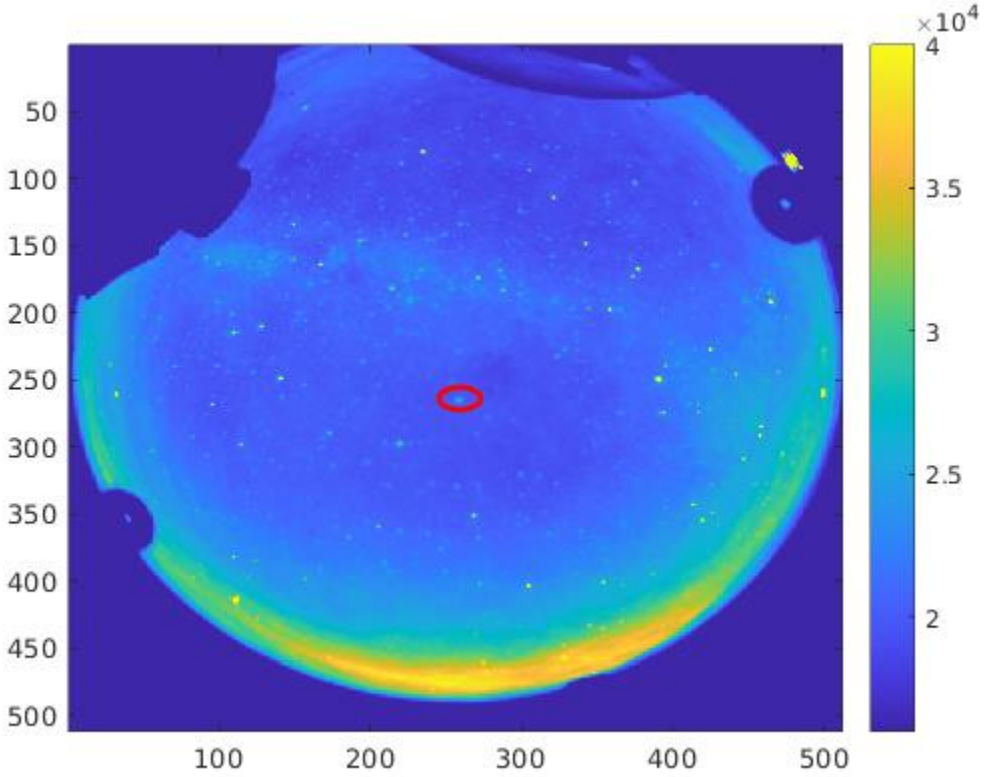

Figure 10: Raw hydroxyl image showing location of Polaris.

The script responsible for identifying the position of zenith and the direction of north, was originally written by Dr. Samuel Kristoffersen. This script requires manually identifying several stars by hand, Polaris for example, and inputting their position in pixels. The script then finds the position of north and zenith through a least-squares fit routine. This is rather

tedious and prone to user error (at least when I used it) through incorrect manual identification of stars.

To improve upon this script, a peak finding algorithm was adapted for use with PASI data. Using a star list, the location of the brightest 100 or so stars are compared to

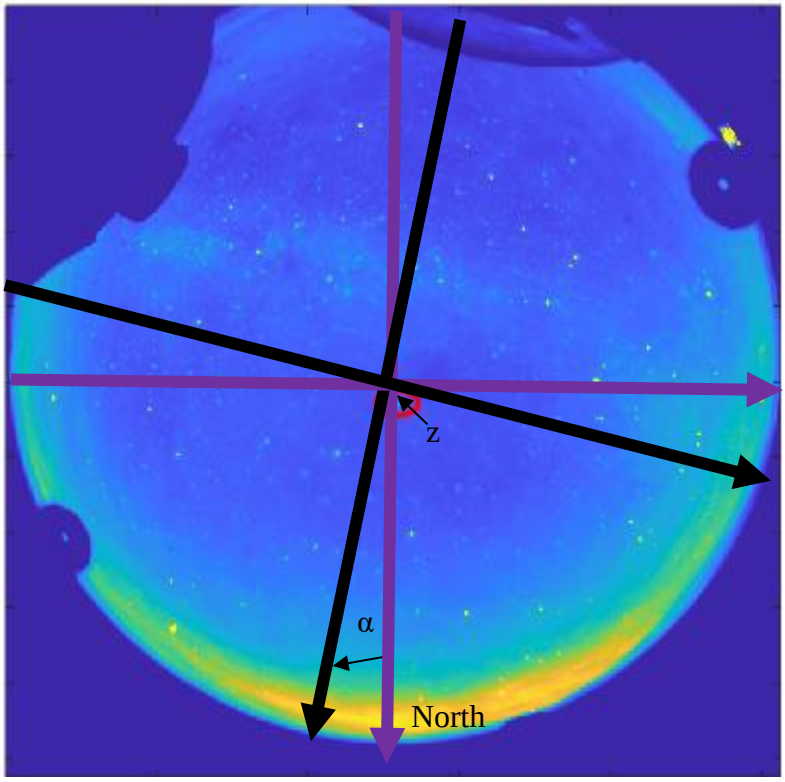

Figure 11: Illustration of location of zenith and north offset on an image of the sky from PASI

the location of the peaks found in the image field of view. Once matched, the list of matched stars is used as the input for the original zenith/north finding algorithm and the output is stored for use later in the calibration routine. The use of a list and peak finding algorithm allows many more stars to be used in the determination of North and Zenith, and minimizes the likelihood of incorrectly identifying a star by eye. The script is run for each

season, and outputs the location of zenith (z), and the angle offset from north (α). An illustrative example of these positions can be seen in Figure 11, and the list of determined zenith and North positions are in Table 4. While the positions of zenith are nearly identical year to year and from image to image, the position of north varies when the instrument is moved, be it for maintenance purposes or otherwise. This has been minimized by using a rail system to mount the instrument. As the rails are fixed, the direction the instrument faces is nearly fixed as well.

Table 4: Location of zenith and north for PASI data

Season	Zenith "x" position (px)	Zenith "y" position (px)	Angle from North (deg)
2009 -2010	262	234	0
2011-2012	261	233	1
2012-2013	262	234	4
2013-2014	262	233	3
2014-2015	261	232	1
2015-2016	260	234	1
2016-2017	259	234	1
2017-2018	260	234	1
2018-2019	260	234	1

Image Sorting and Cloudiness

To calibrate the raw images ($\boldsymbol{I_{raw}}$), they must be loaded into memory and the dark frames ($\boldsymbol{I_{dark}}$) removed, data with different exposure times must be correctly combined, and the background images must be properly aligned with the corresponding data frame. Before the calibration is applied, the cloudiness of each image is calculated. The dark frame is taken with the shutter of the camera shut and subtracted from the data frame. Removal of a dark frame serves to remove any light effects associated with the instrumentation, and not the object of interest (i.e. the sky). These effects include effects such as any offsets applied due to the nature of CCD's (Veselinovic 2011), pixels which are "hot" where the pixel has collected non-airglow signal electrons, and other non-sky signals which are present when the camera shutter is closed. This is in contrast to background images, which are taken of the night sky, but at a wavelength without airglow present. Thus, the removal of dark frames minimizes instrumentation effects, and the removal of a background image minimizes the effects of non-airglow sky signal. The result of this difference is the airglow signal ($\boldsymbol{I_0}$).

$$\boldsymbol{I_0 = I_{raw} - I_{dark}} \quad \textbf{(1)}$$

The "normal" exposure time images in this data set are labeled with "mode_1", and the short exposure time images are labeled with "mode_2". The idea here, is the lower exposure time images allow the observation of airglow deeper into twilight without

saturating the detectors. This is possible because the sky becomes substantially brighter as the sun gets closer to the horizon. To achieve this, the mode 2 images are one fifth the exposure time of the mode 1 images. Thus, five mode 2 images are combined to have the equivalent values. However, it is unwise to just add the five images, first the dark frame is removed from each **(1)** and then the images are added together **(2)**.

$$\boldsymbol{I_0 = \sum_{i=1}^{5} \left(I_{raw_i} - I_{dark} \right)}$$

(2)

The main interest of those who use data from PASI is the airglow and its variability. With that in mind the first correction done is the detection of geophysical events that obscure the view of the airglow. Being a ground based optical instrument designed to study the airglow layer, anything between the instrument and airglow layer will render PASI nearly useless. The known "events" that will obscure the view are as follows: snow, ice, frosting of the instrument dome, and cloud cover. In each of these cases light from above the cloud layer is prevented from reaching the instrument. This includes both airglow, and star light. To leverage this fact, the same star detection routine used to find zenith was modified so that the detected stars could be compared to a list of known bright stars in the sky above Eureka. The output of the routine is the stars which are visible in the current image of interest (Figure 12). Using a set list of 121 stars visible in this field of view, and limiting the set to the brightest of stars, the observable stars can be compared to the number of stars observed (Figure 13). In other words, the sky is clear

when all the stars are visible, and the sky is not clear when the stars are not visible, with varying levels of clear sky in-between these boundaries. The percentage of stars missing from the list are stored for later use/diagnostics.

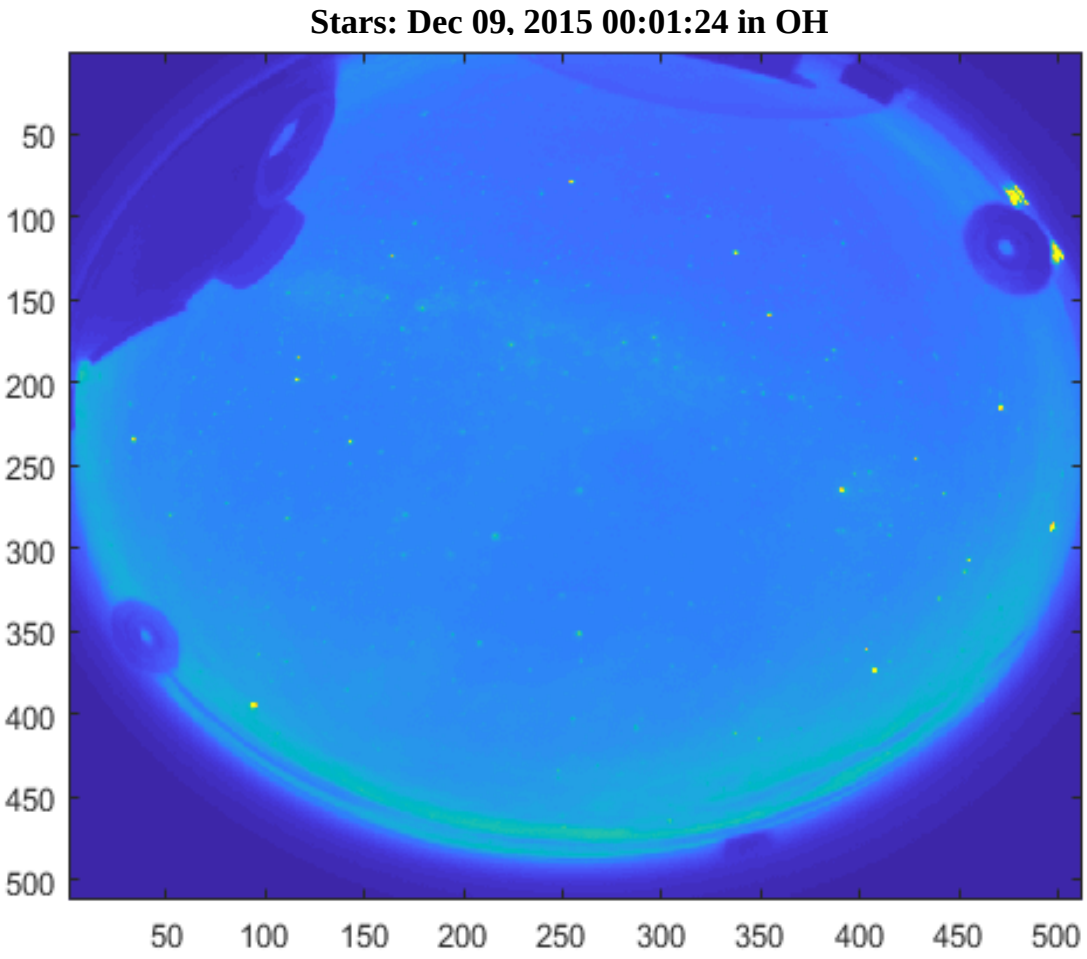

Figure 12: Raw Hydroxyl Image showing stars on a clear day.

Figure 13: Hydroxyl image filtered with several procedurally identified stars circled.

As a preliminary check for validity, the percentage of the stars marked as missing in the PASI data is compared with data from the IR temperature sensor pointed vertically and co-located in Eureka (Sky temperature data provided by Qian Wu, High Altitude Observatory, from the Ridge lab, in Eureka Nunavut). This infrared temperature sensor uses sky temperature to infer cloudiness, with lower temperatures corresponding to clearer time periods. Figure 14 clearly shows good agreement between the fraction of missing stars, as determined from the PASI data set, and the sky temperature as measured by the IR temperature sensor. The temperature increases quickly with cloud cover, and during

periods of notable cloud coverage both PASI and the IR temperature sensor are in close agreement. Where the raw data provided by PASI are images, a visual representation of the evolution of observational conditions can also be used to determine cloudiness, however with an abundance of images in a season (>200,000) using the raw images becomes tedious. However, a visual representation provides convincing evidence that what is being observed is in fact a deterioration of observational conditions, as can be seen in Figure 15.

Table 5*:* Physicalities of a subset of stars used for cloud detection and zenith finding (Dec 9, 2015 00:01:59)

Star	Magnitude	Distance (ly)	Apparent Zenith (Deg)	Azimuth (Deg)	Right Ascension (Deg)	Declination (J2000) (Deg)	Position (pix) [X;Y]
Vega	0.03	25.04	48.8019	260.2843	279.23526	38.7852	[116;199]
Capella	0.08	42.80	44.5050	81.8155	79.17320	45.9960	[391;264]
Deneb	1.25	1411.93	37.5968	229.1185	310.35799	45.2803	[180;153]
Alioth	1.77	82.55	43.4683	342.0902	193.50820	55.96	[209;358]
Mirfak	1.79	506.45	35.9422	108.5070	51.08086	49.8611	[366;209]
Dubhe	1.79	123.64	38.2395	4.0944	165.93109	61.7516	[259;352]
Alkaid	1.86	103.94	49.1251	329.8938	206.88435	49.3131	[175;358]
Menkali-nan	1.9	81.11	47.3391	72.0277	89.88183	44.9474	[391;289]
Polaris	2.02	432.57	9.5440	3.1462	37.95950	89.2643	[258;265]
Kocab	2.08	130.93	23.4273	327.5341	222.67611	74.1554	[216;293]
Schedar	2.2	228.24	24.1413	154.2699	10.12717	56.5374	[296;173]
Sadr	2.2	1832.34	43.1826	233.0284	305.55711	40.2567	[161;149]
Mirach	2.05	197.43	45.4924	149.9048	17.43388	35.6200	[337;122]

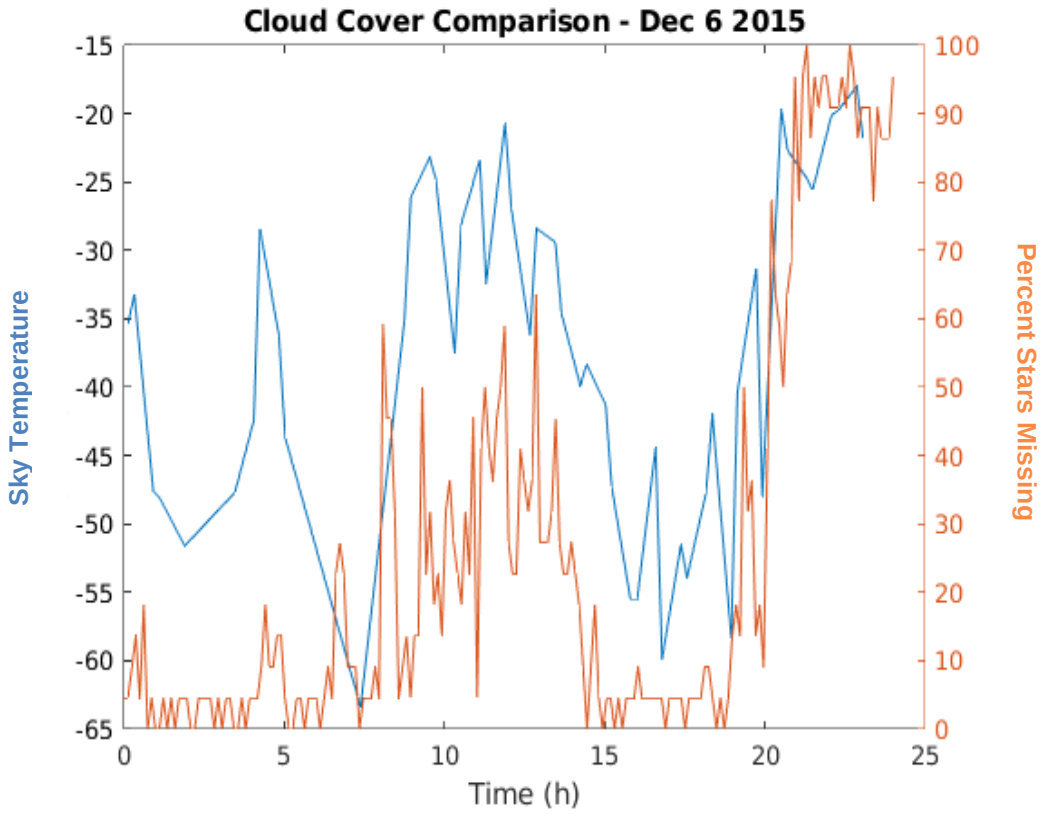

Figure 14: Cloud cover, PASI vs IR temperature sensor

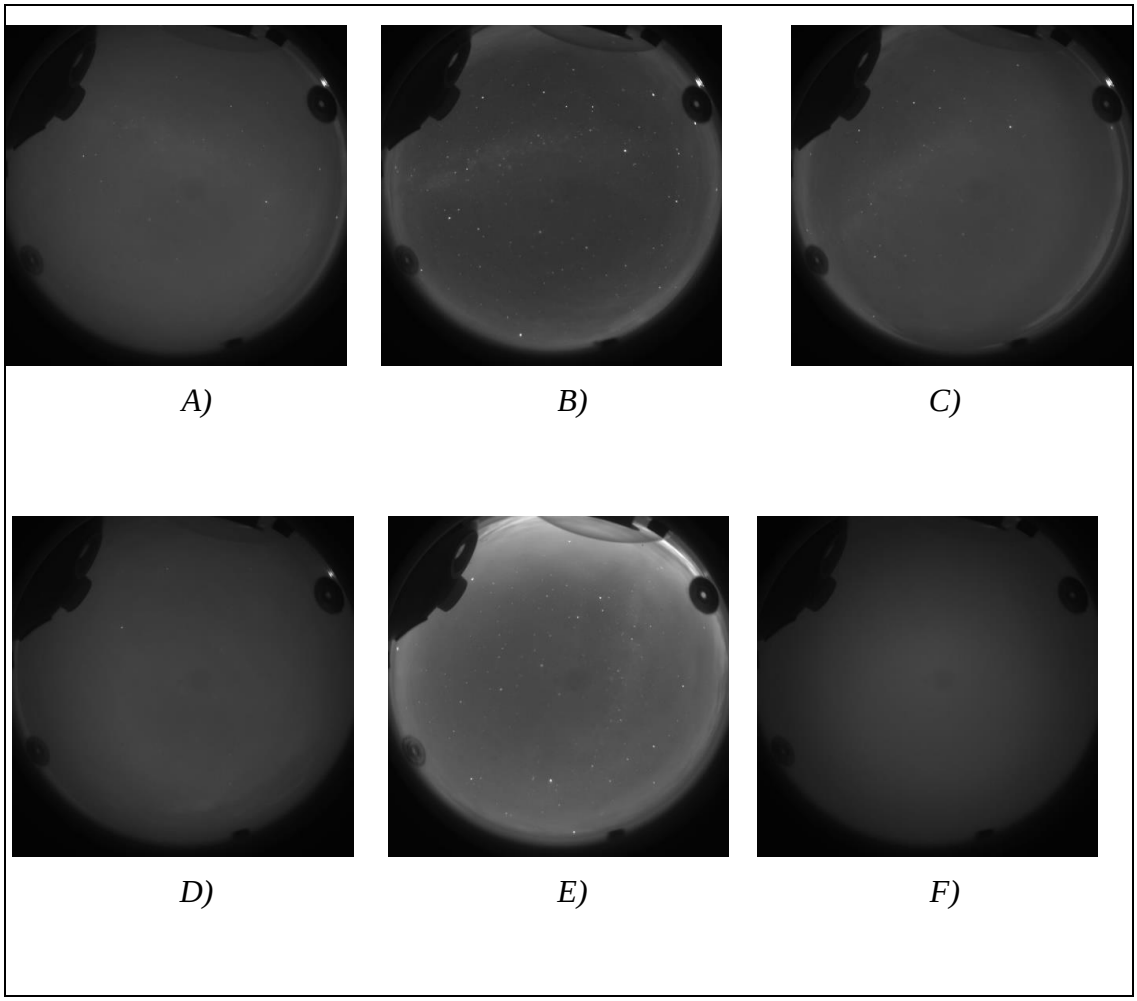

Figure 15: Evolution of sky cloudiness associated with Figure 14 using the hydroxyl (OH) filter. December 6, 2015, at UTC: A) 00:11:05, B) 03:33:23, C) 04:04:57, D) 09:21:59, E) 18:00:46, F) 23:12:09

Figure 15 shows how the sky looked at various time during December 6, 2015. The intent is to illustrate how the real sky relates to these derived values (temperature and % stars missing). Figure 15 panel (a) through (c) are free of clouds, and panel (d) is cloudy. This panel is at 09:21:59 and shows there are greater than 20% stars missing in Figure 14.

Thus, a cut-off of between 20-30 % is adequate for the binary cloudy/clear conditions of interest in this thesis.

Masking and Manufacturer Calibration

To get a clear picture of only the sky elements, the non-sky elements present around the outside of each image are masked out. These elements are the other instruments, buildings, terrain, etc. This process is done manually through thresholding. Using a bright image to maximize the difference between the sky and non-sky regions of the image, the dark non-sky elements are identified and marked by replacing the pixel values with not-a-numbers (nan). Given that the instrument may move between seasons, a new mask is produced manually for each season. The result of this process can be seen in Figure 16.
A calibration routine, complete with calibration constants, was included as part of the documentation provided by the manufacturer (Keo Scientific) of the All-Sky imager.

Application of the calibration is rather straight forward:

$$\zeta(x,y) = \frac{A(\lambda)I(x,y)_{dN}}{Bt(s)_{exp}G} \quad (3)$$

The final output from the calibration is given by ζ, the image in units of spectral radiance, the Rayleigh (10^{10} photons per square meter per column per second). Starting with the denominator; B, $t_{exp,}$ and G (binning, exposure time, and gain) are all constants determined by the user. As PASI has the ability to do on-chip binning, B is determined by the resolution of the image. Native resolution is 1024x1024 pixels, so a binning factor of 4 would be an image resolution of 512x512 pixels. PASI has a gain setting which was set to 1, meaning no multiplication/division of the detected signal. In the numerator are the instrument specific corrections. I_{dN} is a matrix of a values normalized to 1 which accounts for the efficiency with which light passes through the optical system, as well as the sensitivity of the CCD detector. Application of I_{dN} to an image is also known as flat-fielding (Figure 17), where an image of the same resolution as the data is collected in a lab under the conditions of constant brightness. The flat-field image is scaled to the centre pixel brightness, giving the centre pixels the value of 1 with decreasing pixel values towards the edge, as the constant light source is attenuated towards the edge of the optical system. Dividing by I_{dn} increases the edge values by the appropriate constant, so that the final data product is free from optical system related light attenuation. *A* is the absolute calibration coefficient. This coefficient converts the pixel values from unitless counts to Rayleighs, is instrument specific, and was determined in a lab by KeoScientific (Table 6).

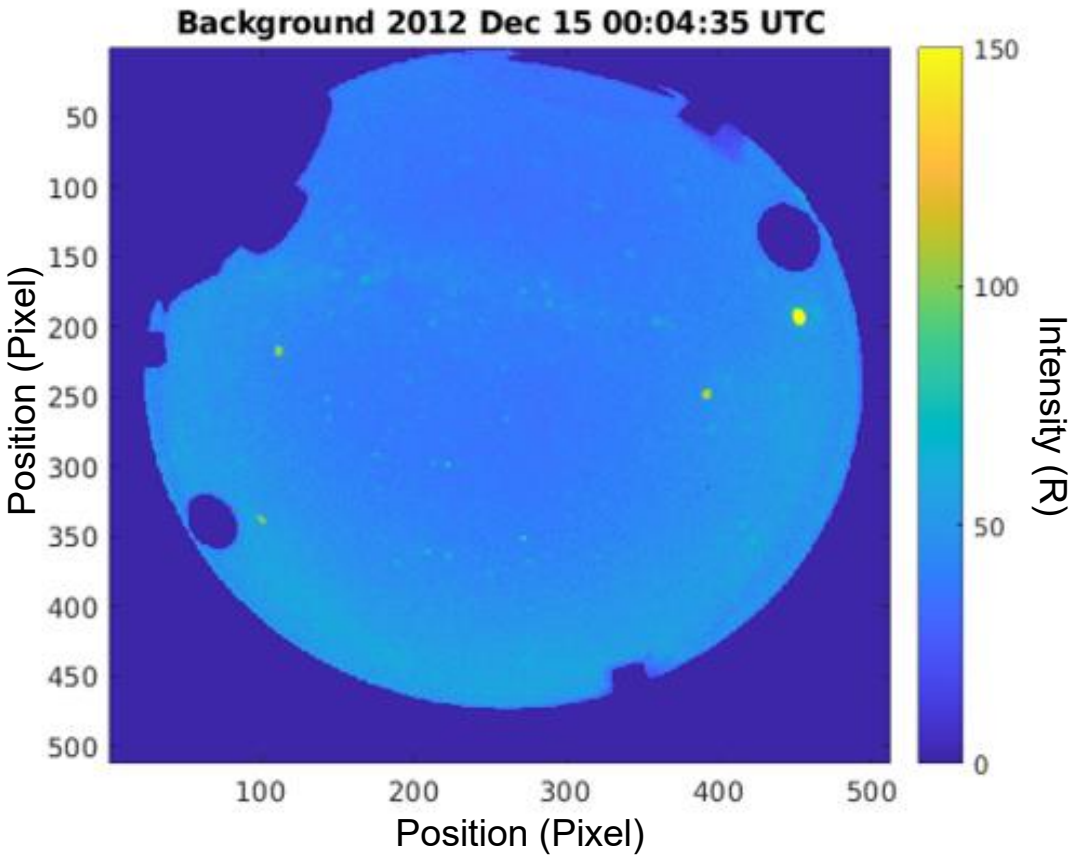

Figure 16: Background image pre-star removal with masked non-sky features

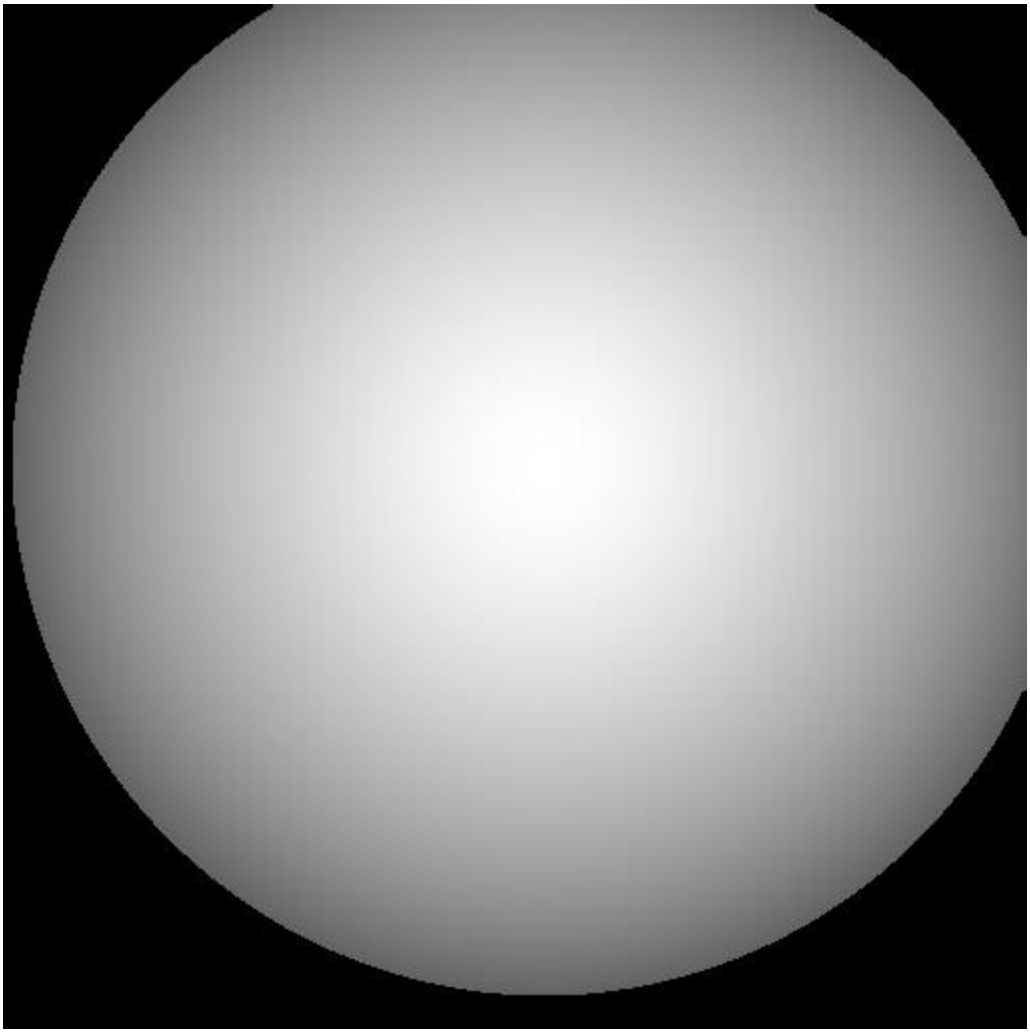

Figure 17: PASI flat-fielding image

Table 6: KEO Scientific calibration coefficients

Camera Lens FoV	Filter Identifier	Effective Bandwidth *(nm)*	Efficiency Factor *(unitless)*	Absolute Coefficient *(R*s / dN*nm)*
180	4278	2.72	0.970	30.3
180	4400 *	9.17	0.992	567824.5
180	5000 *	10.76	0.966	324643.3
180	5577	2.04	0.869	29.5
180	5725	2.05	0.902	20.4
180	5893	2.19	0.799	17.7
180	6300	2.72	0.911	15.3
180	6375 *	10.68	0.997	117173.5

The other values in Table 6 are the effective bandwidth ($\delta\lambda_{Eff}$ and efficiency factor (e). These are properties of the instrument filters and are used in the final calculation of radiance, as shown in (4).

$$L_a = \delta\lambda_{eff}\frac{\zeta_{Measured} - \zeta_{BGMeasured}}{\varepsilon} \quad (4)$$

Both $\zeta_{Measured}$ and $\zeta_{BGMeasured}$ are the output of (3), and $\delta\lambda_{eff}$ and ε are for the emission of interest. For example, if the atomic oxygen green line is the emission of interest, $\zeta_{Measured}$ is the output of (3) for the 557.7nm filter, $\delta\lambda_{eff}$ and ε are equal to 2.04nm and

0.869 respectively. In this case, $\zeta_{BGMeasured}$ is the 572.5nm filter. These equations can be used on a single pixel, or as in this work, entire images. The output L_a is a green line image with units of Rayleighs and the same resolution as the input images. The entire set of images has the calibration applied, with the background, oxygen green line, oxygen red line, sodium, and nitrogen images having units of Rayleighs, and the hydroxyl images having units of counts per second.

Star Removal and Van Rhijn

The stars present in the PASI data set can be used as a tool to assist in the determination of viewing conditions; both manually and programatically. However, the stars are not the data of interest in this work, they are noise to be removed. To do this a filtered image is used alongside the original image and, through differencing, the peaks that are the stars are masked and replaced by the filtered pixels in the same location. This process can be followed in Figure 18, with the result of this process shown in Figure **20**. Figure 19 shows what is expected to be seen in the initial image. Jupiter, Capella, and Vega are all in the expected location. While the process can be modified to improve the removal of stars, the time cost, and potential impact on detecting small scale dynamics, is too great. As is evident in , not all the stars are removed in the final frame, however the "texture" remains within the majority of the image when compared to the initial image.

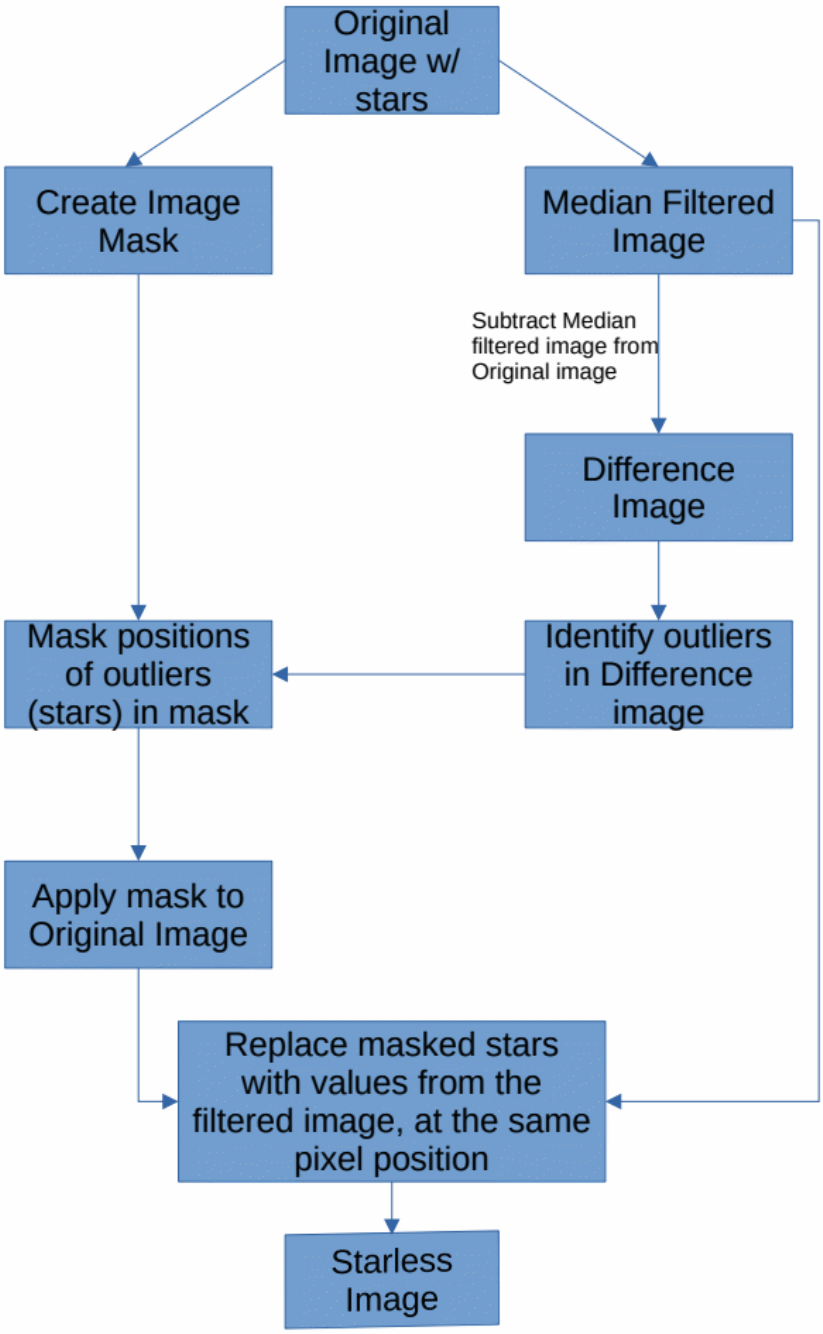

Figure 18: Star removal flow chart

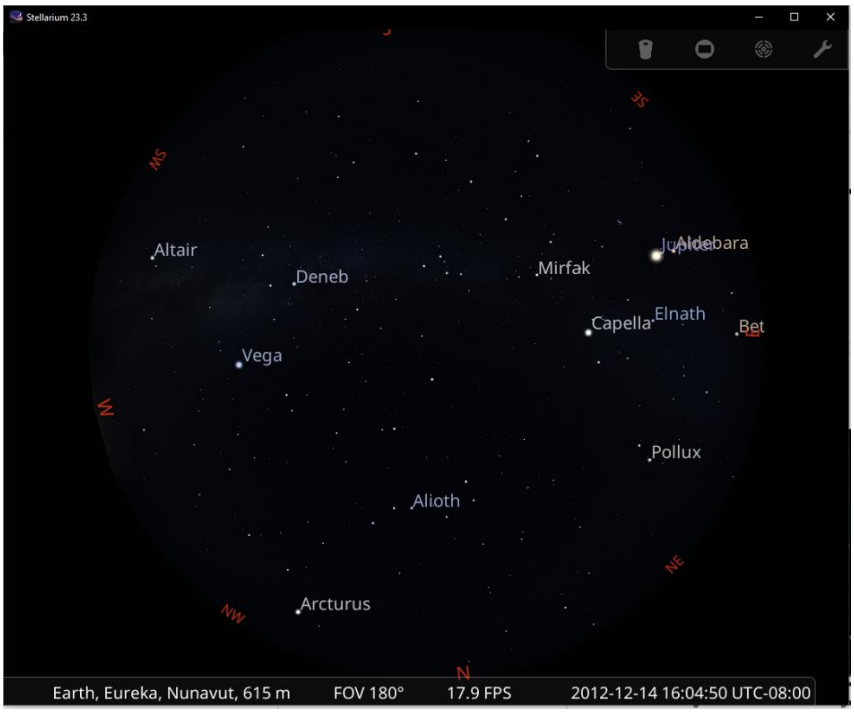

Figure 19: Simulated view of the night sky as seen by PASI on December 15, 2012 at 00:04:55 UTC. Simulated using Stellarium (Zotti et al. 2021)

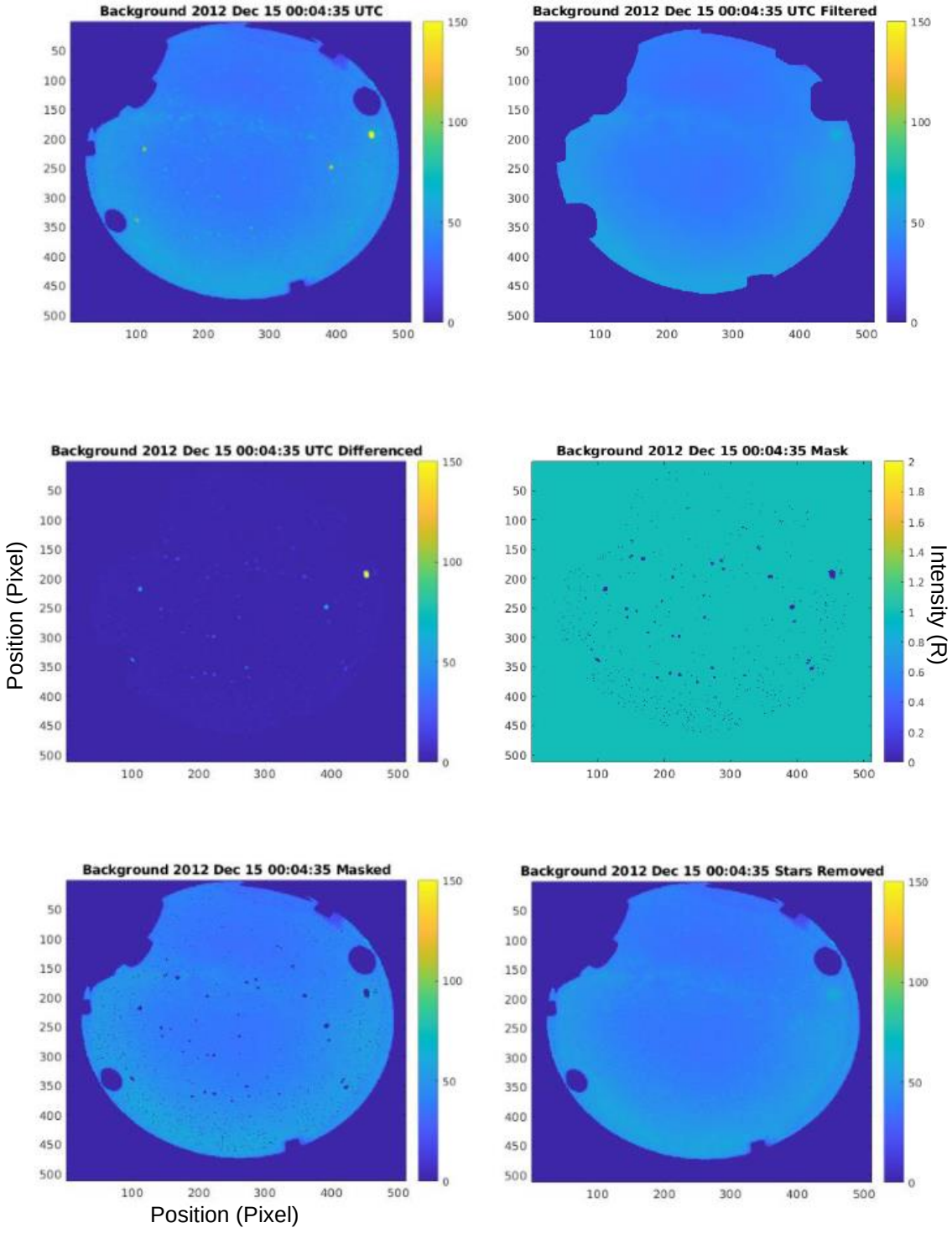

Figure 20: Example results of a star removal

Finally, the Van Rhijn correction can be performed. This corrects for the finite nature of the airglow layer and requires knowledge of the zenith position of the instrument, also known as “up”. Because the layer is finite, the angle of airglow observation increases from zenith, and the observed brightness of the airglow emission increases geometrically (Figure 11). While this approach may be used for the determination of airglow heights (Roach and Meinel, 1955), it is used here for data correction (5).

$$I(\theta) = \left[1 - \left(\frac{R_e}{R_e + z}\right)^2 sin^2\theta\right]^{-1/2} I_o \quad \textbf{(5)}$$

Here *‘I_o’* is the airglow irradiance at zenith and the quantity used for analysis, *‘z’* is the height of the airglow layer in kilometres, *‘R_e’* is the radius of Earth, and *‘Θ’* is the angle from zenith. This equation can be used to correct for the larger path length through the emitting layer, giving a uniform airglow irradiance as if the “slice” of atmosphere being measured is the same in all directions. For this method to work, the height of the airglow layer must be known, and the thickness of the region of brightest emission must be small relative to the rest of the atmosphere. However, for the purpose of calibrating the All-Sky imager, variations in airglow height have a small effect on the correction factor, namely for zenith angles up to about 60° (Figure 22). In the case of this work, the field of view is much more restricted than 60°, it is somewhat less than a 10° field of view thus a large uncertainty in the airglow emission height is negligible.

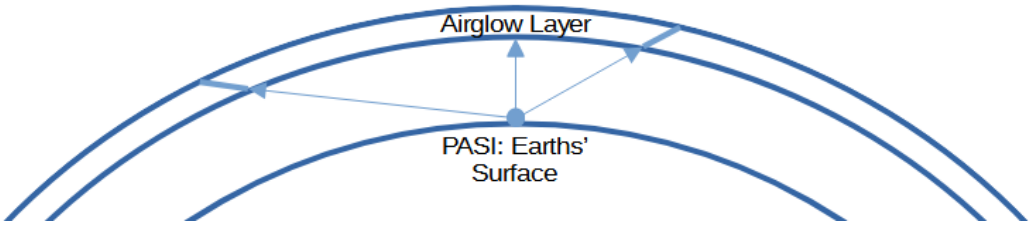

Figure 21: Line of sight through the airglow layer gets longer as the angle from zenith gets larger.

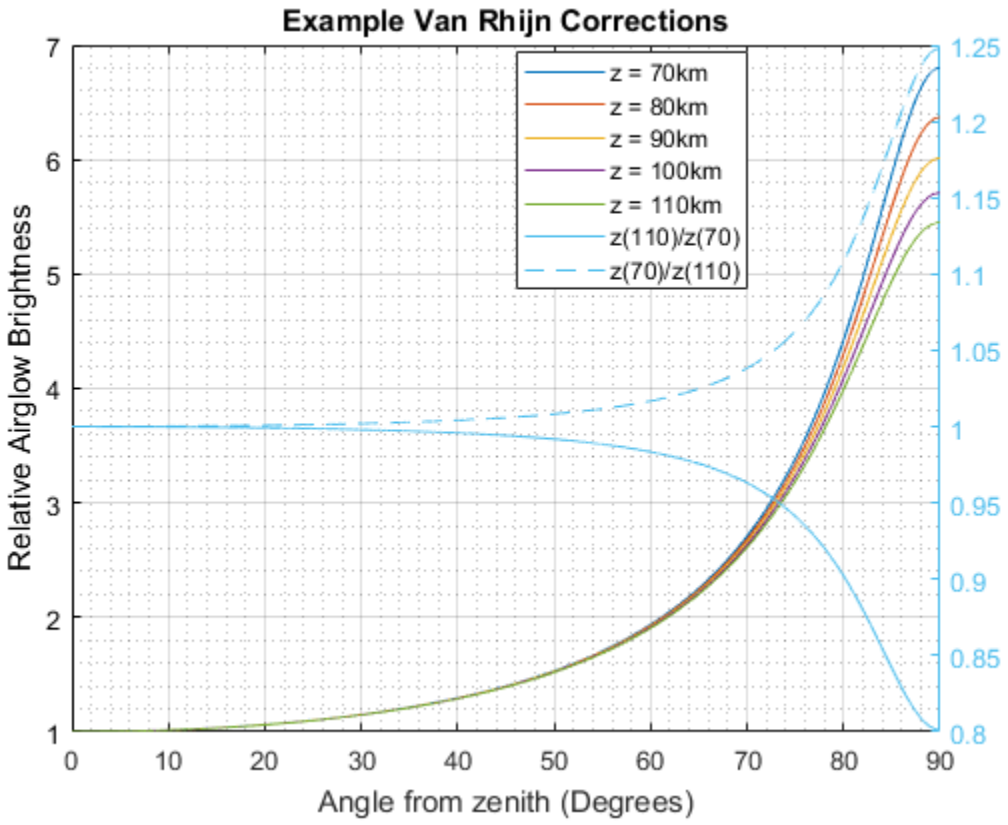

Figure 22: Van Rhijn corrections for various layer heights

Aurora

While beautiful, the presence of aurora in the field of view of PASI is problematic. As noted previously, the green line airglow emission occurs at the same wavelength as green aurora and cannot be removed from a data set by simply choosing a different filter. Instead, it is possible to use the knowledge that aurora is a very bright and short-lived phenomena compared to airglow. In some cases, aurora is so bright, its presence will scatter into neighboring pixels in the field of view. To combat this, a combination of detrending, and outlier detection is used. The following steps are taken to determine the presence of aurora:

1. An image is separated into 256 equal bins and the median is computed for each bin. This is repeated for every image.
2. With all images identically binned, each bin can now be plotted as a time series, and detrended through differencing.
    a. Stationarity is checked, and differencing is repeated if required.
3. Any point within the detrended time series below the 2.5% quantile, or above the 97.5% quantile, is marked as an outlier. This is repeated for each bin, creating 256 total detrended timeseries, with independently marked outliers.
4. Whenever 10% of the bins for an image are deemed outliers (chosen through testing) that image is said to contain aurora.

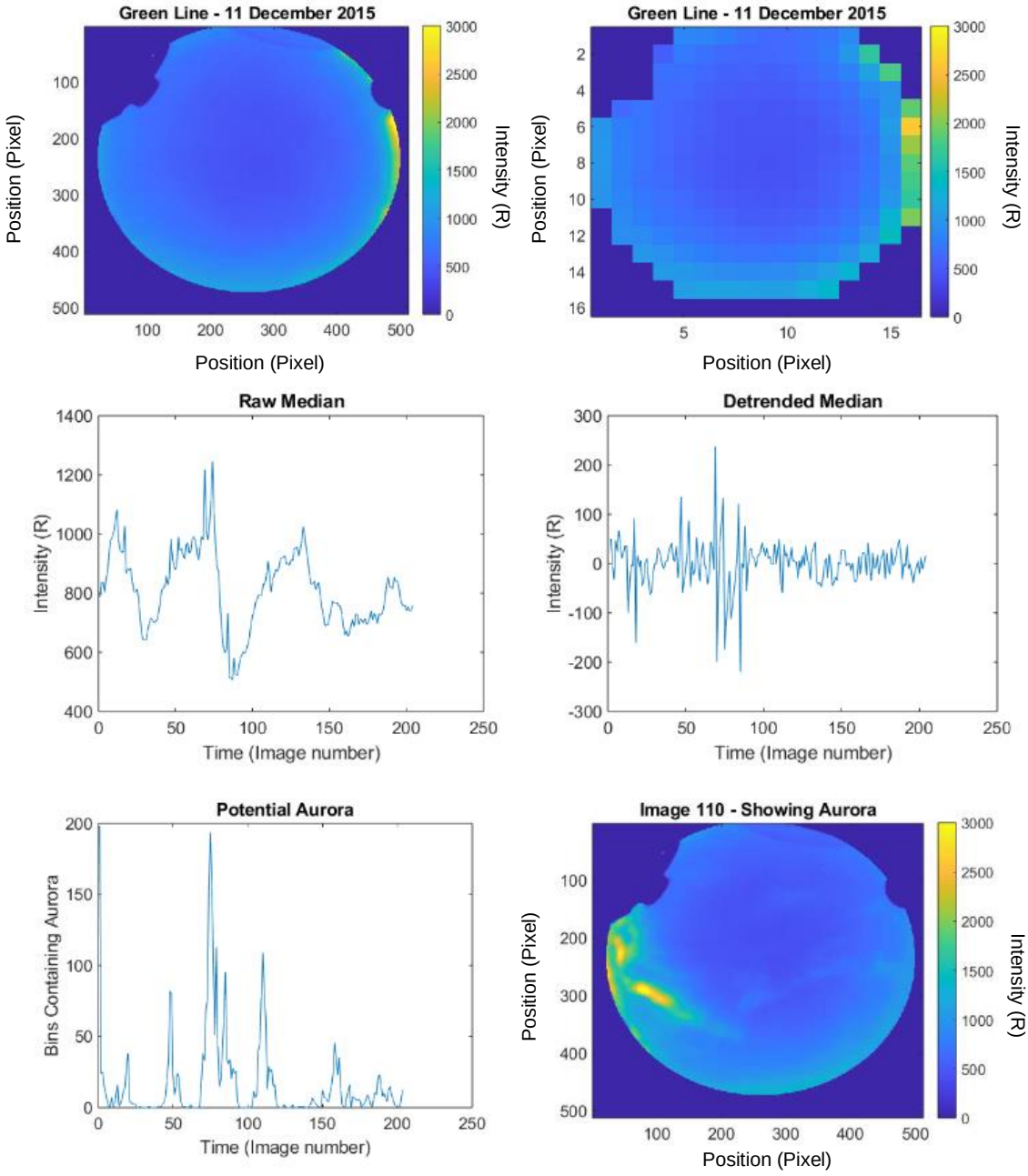

Figure 23: Example aurora removal

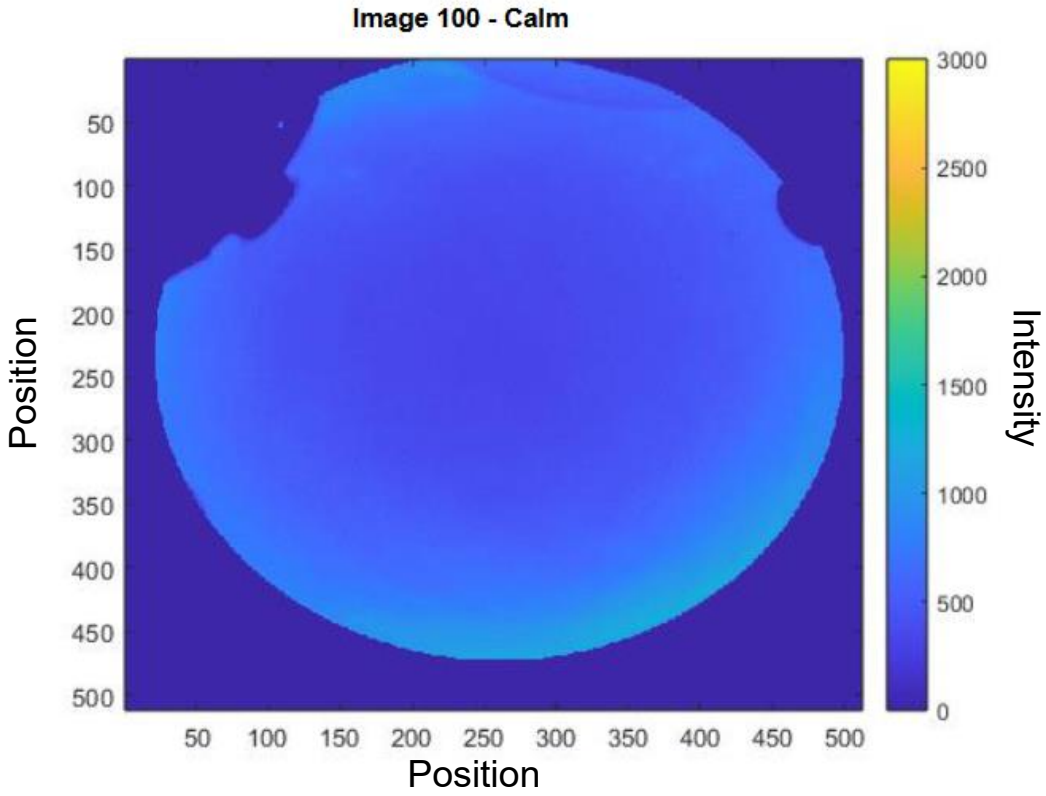

Figure 24: Calm image

The comparison of images 110 and 100 clearly show the difference. This information regarding the presence of aurora is stored as an array, with the index adjusted based upon the number of differencing steps required to achieve stationarity. This ensures that the potential aurora index aligns with the respective image.

Atmospheric Extinction Consideration

The final consideration in the process of calibration and correction is the atmospheric extinction. Light from the airglow layer passing through the atmosphere to PASI is attenuated by the atmosphere and any aerosol present in the atmosphere. This is a complex phenomenon often measured by star photometers (Baibakov et al. 2015; O'Neill et al., 2016; Perezramirez et al. 2008), but for the purpose of this thesis, atmospheric extinction will be entirely represented by Beer-Lambert's law:

$$I(\theta) = I_{true} e^{-\tau_i m(\theta)} \quad (6)$$

Here the actual airglow irradiance, I_{true}, is given by the measured irradiance at angle θ from zenith, the sum of all the contributions to optical depth (τ_i) and the relative mass index (m) at a given angle θ from zenith. For zenith angles less than 80° where moderate levels of accuracy are required, the relative air mass function for a plane-parallel atmosphere is appropriate Figure 25. This range of zenith angles clearly includes our desired field of observation of 60°, and is thus given by the simple relationship:

$$m(\theta) = sec(\theta) \quad (7)$$

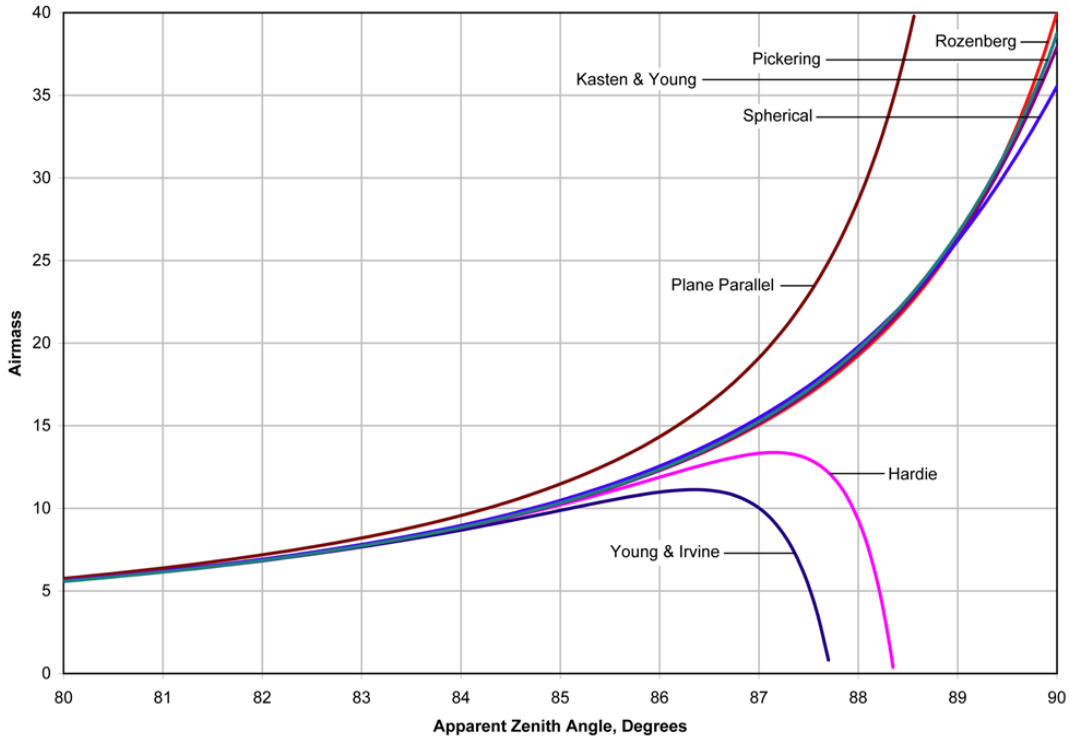

Figure 25: Comparison of different relative airmass models, adapted from Jeff Conrad: https://creativecommons.org/licenses/by-sa/3.0/deed.en

While there are many contributions to the optical depth τ; Rayleigh scattering, aerosol scattering, etc, none of these are calculated and are instead lumped in as a "total optical depth". If one were to be interested in the determination of optical depth and its variation, aerosol optical depth accounts for the majority of variations and would be the main object of study. For a more in-depth discussion of optical depth and photometers see (Baibakov et al., 2015; O'Neill et al., 2016) and others. Without consistent measurements of optical depth, it is difficult to include a correction for the data set on an image-by-image basis. One possible approach to implementing a correction would involve combining

estimates for the two most prominent sources of light attenuation: Rayleigh Scattering and Aerosol Scattering. For Rayleigh scattering the values can be simply extracted from Table 7 for the wavelength(s) in question. For aerosol optical depth, it is possible to find the average of some time-series of aerosol optical depths and decide whether the variability is worth including.

Figure 26 shows an aerosol event with three peaks; two peaks are around a value of 0.2 and one is around 0.3. Assuming each peak lasts one hour during the eight-hour event, the aerosol optical depth is 0.15 on average. Combined with Rayleigh optical depth the resulting correction, using (6) and (7), would be 0.7914. This suggests that every data point is only reported as 80% of the "true" value. However, two "techniques" are used to alleviate this: normalizing by the average and averaging the data into 1 hour or greater bins. This removes the offset imposed by the decision to neglect a constant factor and minimize the effects of aerosol optical depth variations. Therefore, it will be assumed that variations in the observed brightness due to any variations in optical depth will be considered negligible for the work in this thesis.

Table 7: Rayleigh scattering effect, adapted from (Bodhaine et al. 1999)

Wavelength (nm)	Rayleigh Optical Depth	Percent "True" brightness at Zenith
555 (~ Oxygen green line)	0.0935	0.9107
570 (~ Background)	0.0839	0.9195
590 (~ Sodium)	0.0729	0.9297

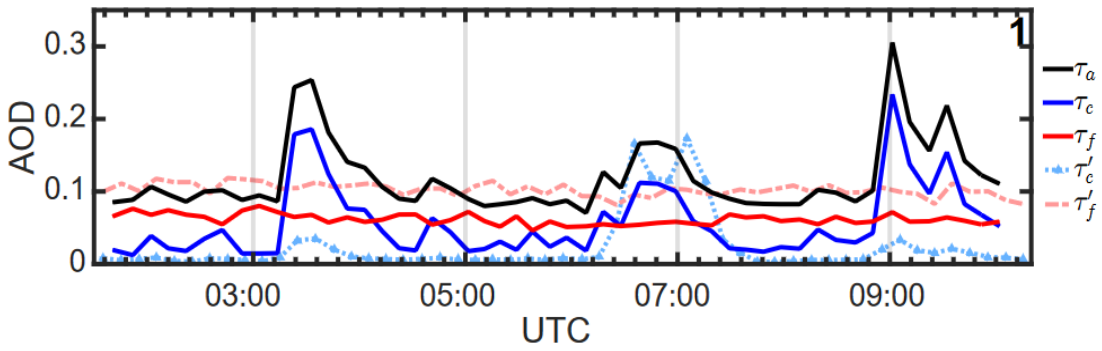

Figure 26: Aerosol Optical Depth (AOD) March 10 adapted from (32)

In summary, each raw image used in this work has the following corrections applied to create the final corrected image: dark frames are removed, mode 2 images are combined, data images are temporally aligned with background images, cloudiness and aurora are determined for later use, scene elements are masked, the manufacturers calibration is applied, stars are removed, and the VanRhjin effect is corrected for.

Image and descriptive data storage

With the corrections and organization complete, images are saved to the hard drive along with any values calculated for that image. The output is a .png with data type uint16, values with units of Rayleighs, and a corresponding .mat file for the day with the following column labels:

aurora	pot_aur	cloudy	cloudiness	TIME	extinction	extinction_err	air_MAG	RMSE	R2

The first 5 columns are the only columns which are to be used at this time. In order these columns contain:

- A binary indication of the presence of aurora
- The number of bins with aurora suspected
- Value of cloudiness indicating the number of test stars not visible in the image
- A binary indication if the image is too cloudy to be used
- The time which the corresponding image was saved in date number format

The final 5 columns are related to a calculation of optical depth that was implemented but found unreliable. In short, the idea is this: there are several bright stars with stable magnitudes within the field of view of PASI. Knowing what these magnitudes are "supposed" to be, an algorithm adapted from (Baibakov et al., 2015) used for calibrating star photometers, was used to estimate the optical depth. Unfortunately, the output was unreliable and therefore not used in this work. While neglecting the optical depth correction is not ideal, the data is normalized and averaged over time (as mentioned

previously) minimizing the effects of this negation. The framework for exploring all-sky imager star photometry is still in place for anyone who wishes to revive it.

Storing the data in this way allows each day of images to be accessed with the derived information (e.g. cloudiness) simultaneously and with a similar naming convention. These images and mat files will be loaded later to be used in a variety of studies, from atmospheric dynamics to the analysis of the airglow itself.

Chapter 3: Airglow Variability in the Arctic: A decade of observations

This section explores the variations in the sodium, and oxygen green line nightglow emissions. Here, a small section of each calibrated image, located roughly at local zenith, is sorted by different time scales, and periodic geophysical phenomena. The data is further reduced to only include images where the moon is below the horizon to minimize systemic increases in sky brightness caused by the lunar cycle. A clean, calibrated, data set such as this one is the starting point for many airglow and atmospheric dynamics studies. Coupled with the knowledge that other instrumentation co-located at PEARL in Eureka exhibit similar variations, in similar quantities, the foundations are laid for many interesting studies. In this thesis, one example of this new capability will be presented using data from PASI; trends in the airglow emissions over the following scales: solar elevation, diurnal, season, and solar cycle.

Given the large number of data points in this data set (~50,000 “clean” images), it is necessary to combine individual measures of intensity to best exemplify the variations of airglow emissions. Specifically, data near zenith will be extracted from each image, categorized, and combined to create figures illustrating the average behaviour of the Sodium and Atomic Oxygen Greenline airglow emissions. This essentially reduces the entirety of the data to a series of datasets analogous to the more familiar surface weather datasets used to calculate the climatology of surface weather patterns. In the case of this thesis, the data set consists of 10 years of airglow intensities.

The calibrated images are combined based on different time scales such that changes to the brightness of the airglow can be analysed over solar cycle 24, as well as seasonal, diurnal, and solar elevation related changes. As alluded to in the section on airglow variability, these robust variations can be explained by the dominant physical phenomena at different time scales. Due to the nature of the polar regions of Earth, there should be no appreciable direct effect of ultra-violet radiation from the sun on the production of atomic oxygen, and thus airglow, locally. It logically follows that if variations in the airglow during polar night are not being influenced by the production of atomic oxygen, variations must be due to the transportation of atomic oxygen from elsewhere in the atmosphere.

As much of the work done in airglow research has been focused away from the polar regions the high arctic trends are compared to similar trends in the airglow observed at much lower latitudes by (Hart, 2019) using the BOSS (Baryon Oscillation Spectroscopic Survey (Smee et al., 2013) in New Mexico, which has measurements spanning the same years as PASI. This illustrates the similar structure of airglow variability between the vastly different latitudes, but also the need to consider how the phase of different tidal phenomena is affected by the difference in latitude. Plot from (Hart, 2019) include data from SDSS. This is an older mission co-located with BOSS, however there is no temporal overlap in the SDSS and PASI data sets, and thus will be ignored in this work.

Data Preparation

The data that will be used to look at trends in the high arctic airglow data set *could* come from any location in the field of view of PASI. The choice determines the geographic location above which the airglow is measured. As the data location moves away from zenith, the uncertainty in the measurements increases as the viewing conditions becomes increasingly difficult to approximate, and the Milky Way moves through the field of view when the angle of observation is greater than ~10 degrees. To keep the analysis simple the data points used are from the pixels centred on the location of zenith. The process used to prepare the zenith airglow emission values follows:

- Isolate the viewing window.
- Determine the solar elevation demarcating the onset of twilight based on convention and rapid increases in emission rates, to then limit the data to night only.
- Bin and average the data to explore trends at the desired timescales:
    - Solar elevation dependence
    - Seasonal
    - Diurnal
    - Over a solar cycle

Each data point is composed of the collection of 225 pixels that make up the zenith position of each image, as seen in Figure 27 and Figure 28. To avoid the assumption that the data is normally distributed bootstrapping will be used to resample the data 10,000 times, calculating the mean for each resample. The result is a distribution of means, the

standard deviation of which gives the standard uncertainty and best estimate of the central tendency for each measurement of zenith.

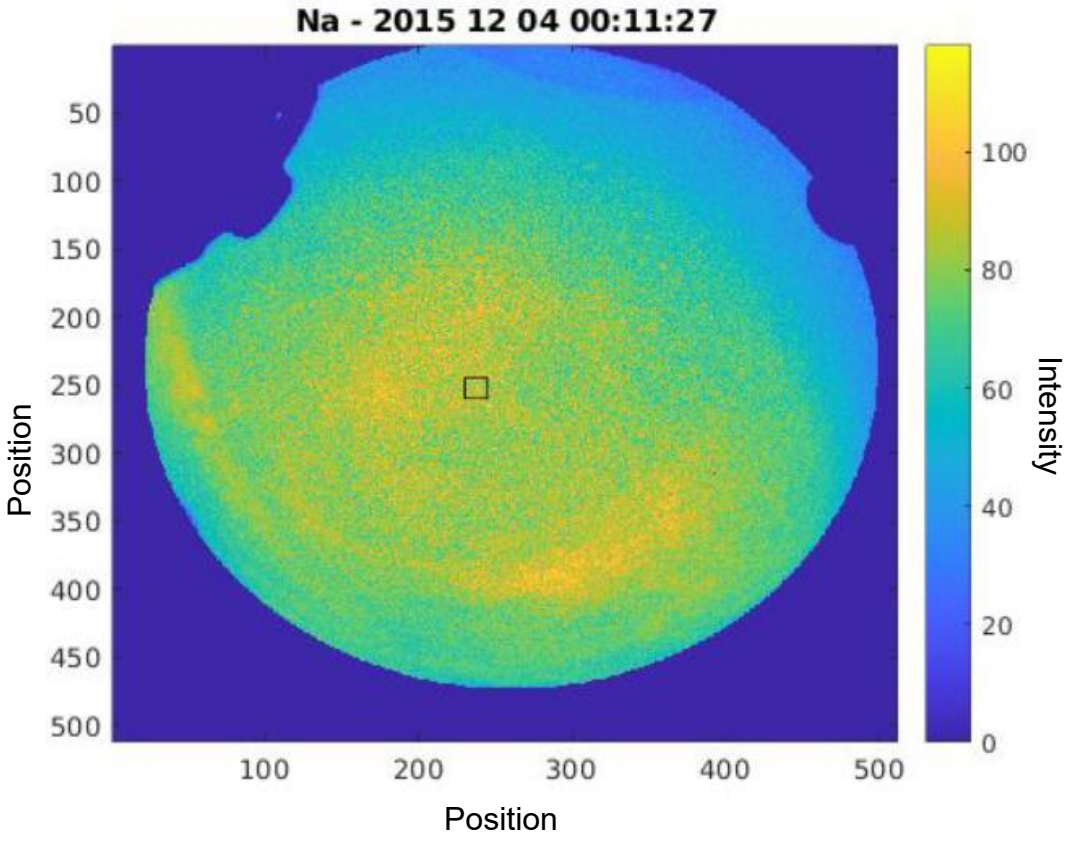

Figure 27: Example image showing approximate location of zenith

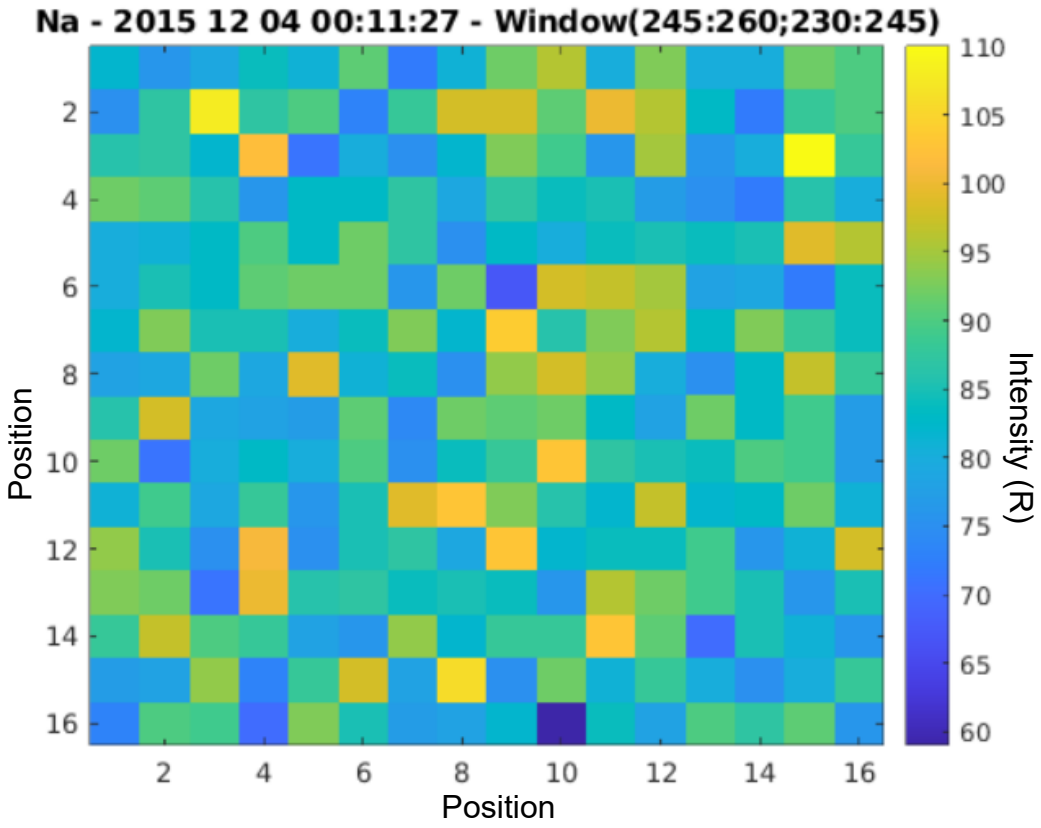

Figure 28: Zenith window selected for processing

Next, the individual data points are categorized and averaged according to the solar elevation at PEARL when the data was first collected. This data is used to determine the solar elevation at which the airglow ceases to be nightglow and begins to be twilight glow. In this work, nightglow has been chosen to occur when the sun is 18 degrees below the horizon or more. As for the solar elevation plots, the newly restricted data are combined again; this time using the median for plotting the airglow emission rate computed diurnally, and seasonally, while yearly data points are computed using the mean. These trends are plotted for nighttime solar elevations exclusively, and the representation of the central tendency chosen such that direct comparisons with other data sets is possible. Again, the

goal of this section is to provide convincing evidence that, despite the absence of direct solar influence at high latitudes in the winter, variations in the airglow layer occur and are not random. The data from PASI presented here occurs during solar cycle 24.

Each data point derived from the PASI data set is presented with the 95% confidence intervals in the mean, or the median where appropriate for comparison (i.e. comparisons with data from (Hart, 2019)). In other words: each data point is computed using the mean (or median) of all the points that correspond to that data bin (e.g. the sodium emission with the sun at 20 degrees below the horizon). The confidence intervals are computed as the stand deviation in the mean (SDOM), or 1.58 times the inter quartile range for cases of the median (McGill, Tukey, and Larsen, 1978), and thus represent the confidence in the mean rather than the spread of the data.

Solar Elevation Variations

To ensure the data set is devoid of twilight and twilight airglow enhancements, thus containing only nightglow, the average airglow intensity as a function of solar elevation is plotted, with each data point being the averaged into 1-degree bins. If the brightness shows a trend, particularly an increasing trend towards sunrise (the sun moving closer to the horizon), it suggests something is driving the increase. In this data set, since the background is removed from each airglow channel, it is highly likely the observed increase is caused by photo dissociation from solar radiation, resulting in a higher airglow emission rate. Looking at a plot of measured sodium and green line intensity versus solar elevation (Figure 29, Figure 30 respectively) it is clear that "twilight airglow" is becoming a dominant factor in the measured intensities. Interestingly there appears to be a linear trend in sodium airglow until 18 or so degrees below the horizon, with green line intensity remaining relatively flat over the same range.

Other curious features include the odd changes near the lowest solar elevations: a bump in sodium (Figure 31) and a dip in the green line (Figure 32). It is possible these are artifacts caused by the low number of days at these extremely low elevations, and biasing towards midnight only data points (as opposed to the larger range of times at other elevations), as evident in Figure 33, and Figure 34, where dates between the two lines represent those included. For this work these features are noted with an orange arrow, as investigation is warranted, but they shall remain a topic of future work. With the data restricted to nightglow only, the analysis of night-time trends is now possible.

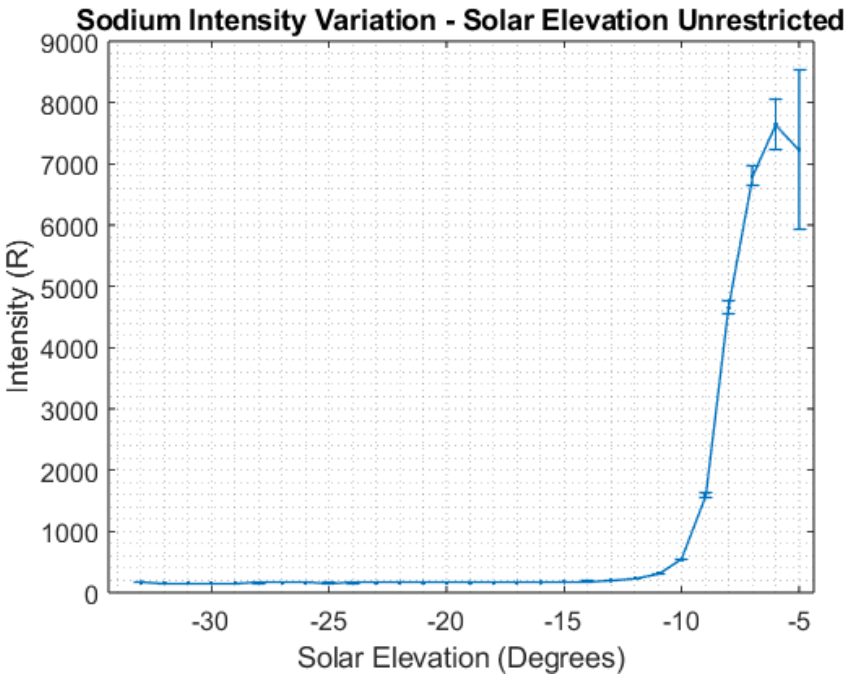

Figure 29: Sodium, unrestricted solar elevation

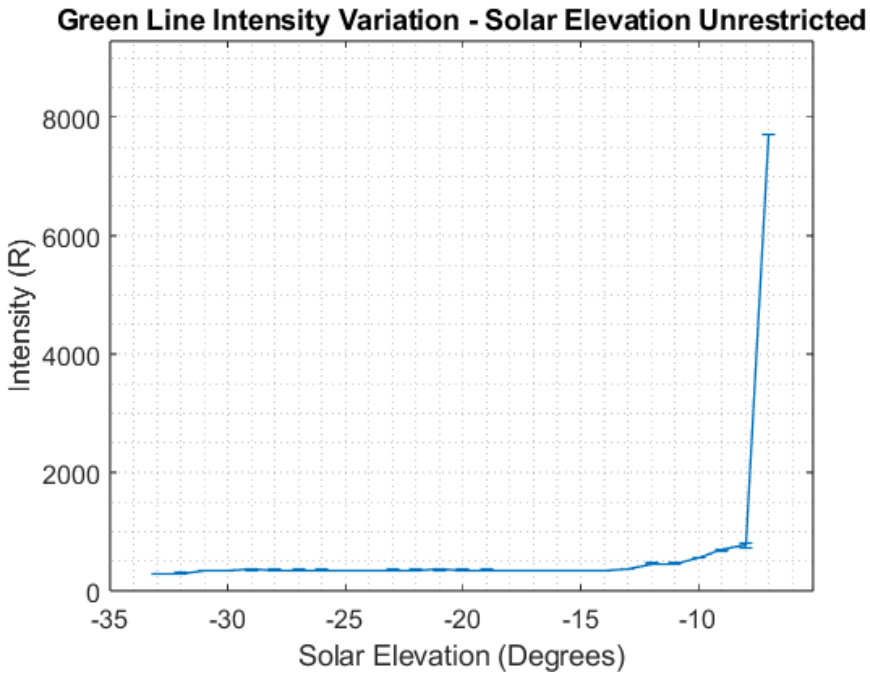

Figure 30: Green line, unrestricted elevation, the "jump" corresponds to a bin with only 7 data points, whereas the others have more than 2000

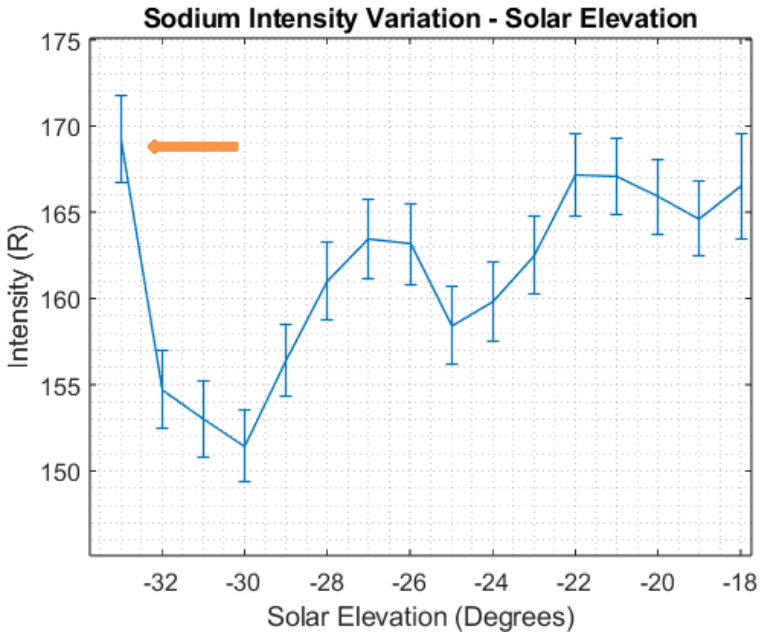

Figure 31: Sodium restricted elevation indicating location of interesting feature with an orange arrow

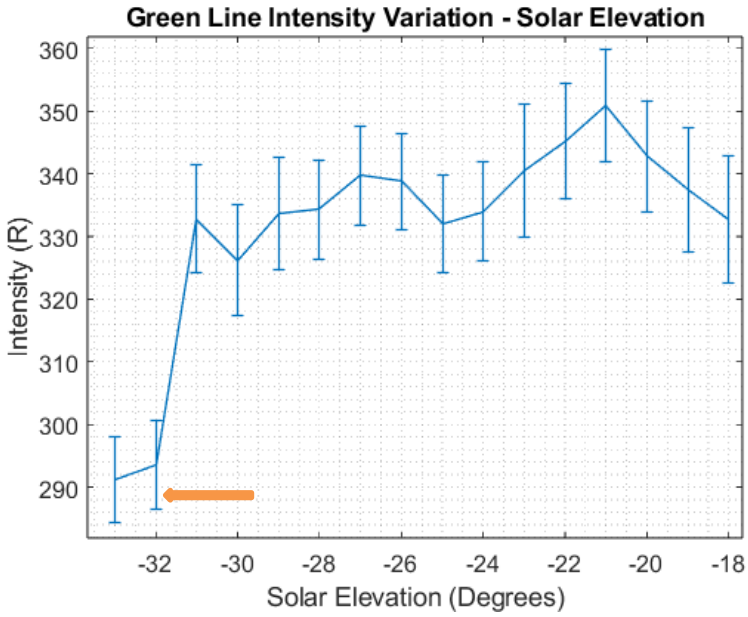

Figure 32: Green line elevation restricted indicating location of interesting feature with an orange arrow

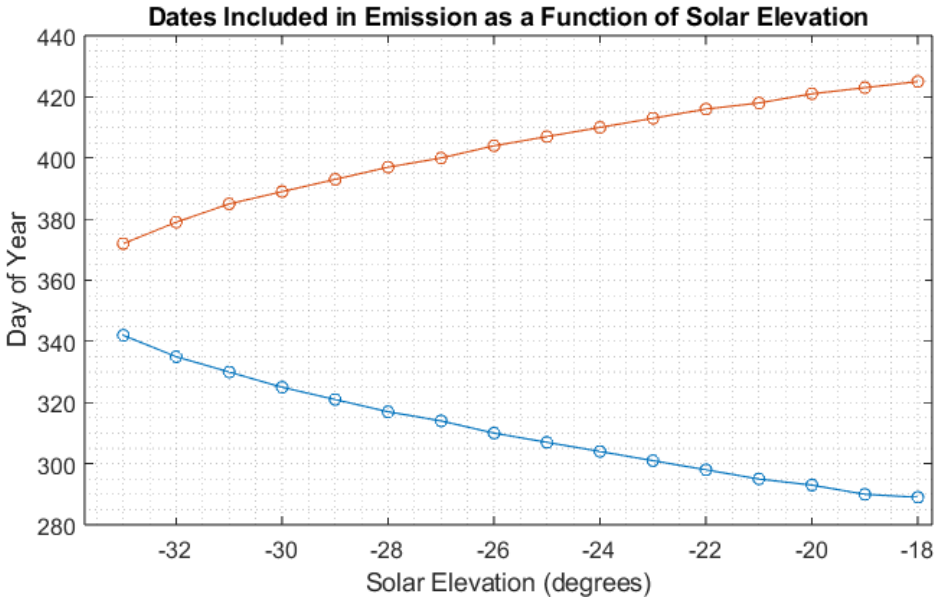

Figure 33: Range of days included at solar elevation, with the orange line being the upper range, and blue the lower range

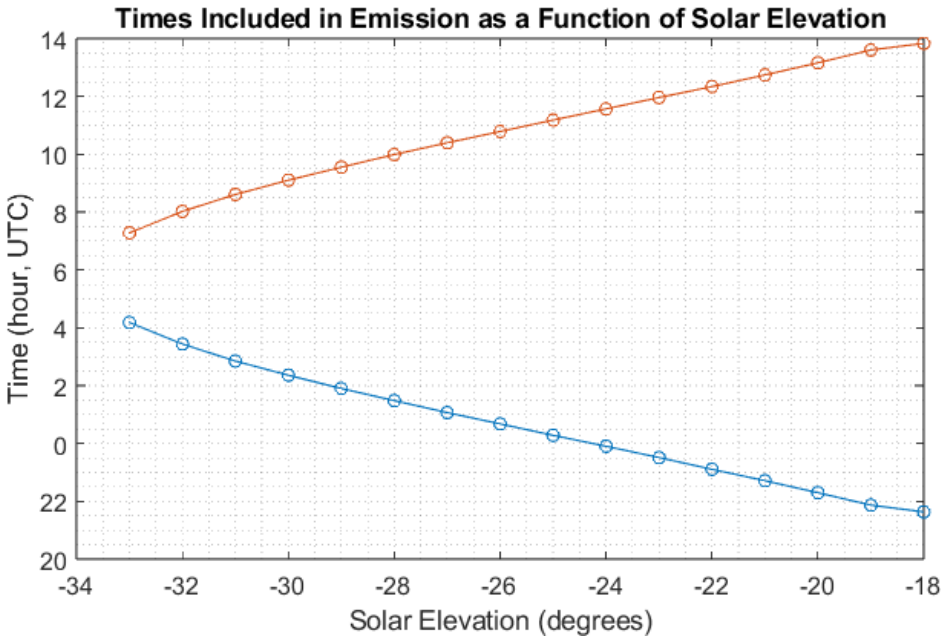

Figure 34: Range of hours included at each solar elevation, with the orange line being the upper range, and blue the lower range

Seasonal Variations

Constituent transport is one driving factor of airglow emission variability. Throughout the year different parts of the atmosphere receive varying amounts of solar radiation, with the poles receiving the least in the winter months. If there were a complete absence of constituent transport, particularly that which occurs pole to pole, airglow emission rates could be expected to decay over the winter months as the reactants are depleted, until the sun once again begins to generate reactants (namely atomic oxygen) late in the winter. To investigate this, data from PASI binned daily and smoothed over. Instead, what is seen is a peak in emission rates in November, with several recoveries in emission rates, and a decreasing trend as the winter progresses, consistent with the absence of local atomic oxygen generation (Figure 35).

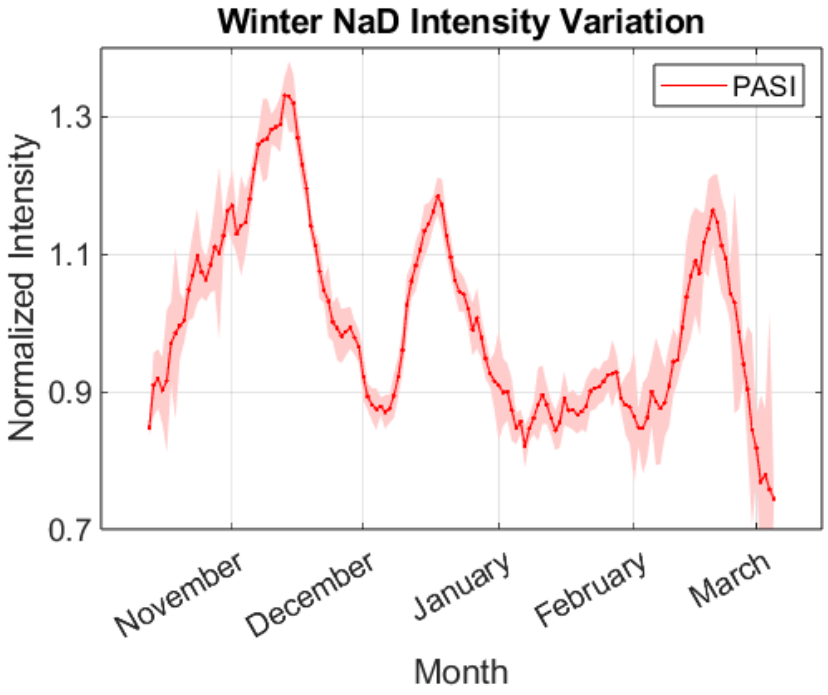

Figure 35: Smoothed PASI annual NaD (589.3nm) emission intensity variations

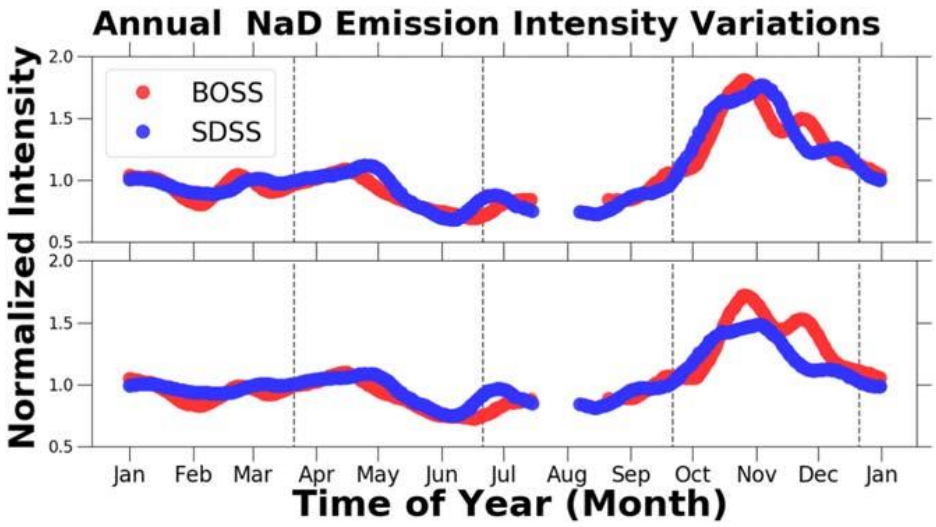

Figure 36: BOSS NaD (589.0nm on top, 589.5nm on bottom) annual variations (Hart, 2019)

Figure 35 and Figure 36 show very similar patterns, despite the data sets being separated by 48 degrees latitude, with the mid-latitude BOSS variation being a bit larger. At first glance it may be tempting to correlate these peaks or recoveries to the lunar phase, but data with the moon above the horizon have been removed. Instead, it's clear that the November and December peaks occur approximately 15-17 days later in the PASI data set than the BOSS data set. This time difference is indicative of the time required for reactants to be transported to the arctic during northern winter.

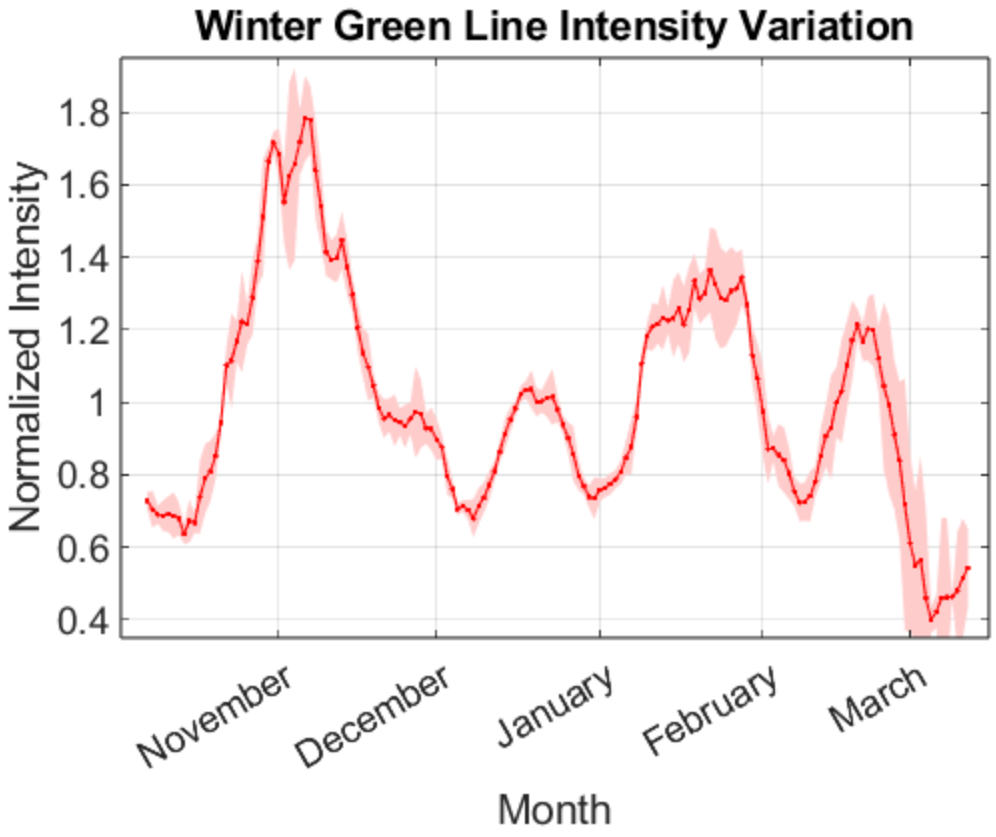

Figure 37: Smoothed PASI annual green line (557.7nm) emission intensity variations

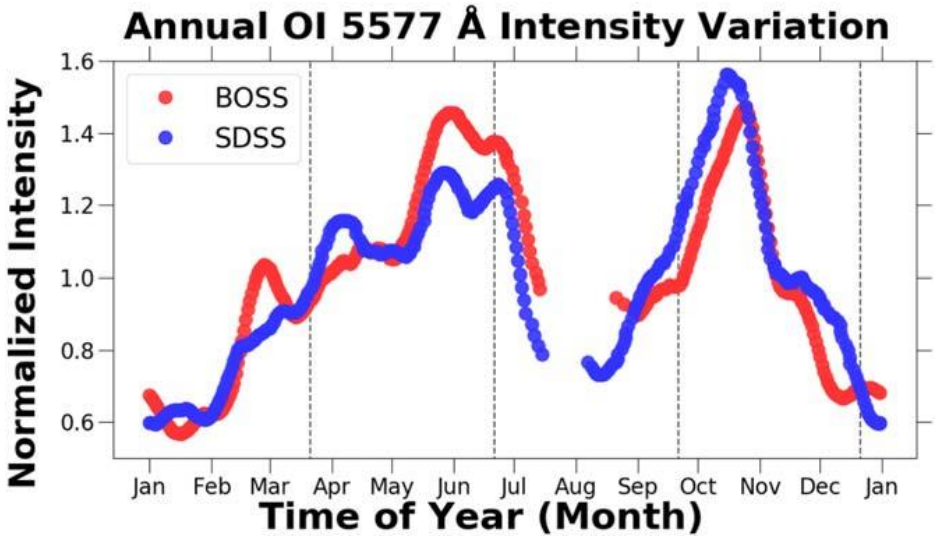

Figure 38 BOSS green line (557.7nm) annual variations (Hart, 2019)

A similar situation exists for the oxygen green line emission (Figure 37, Figure 38), with the emission peak in the high arctic data set occurring approximately 8 days after. Comparing the timing of the two emissions in the PASI dataset, the NaD November emission peak occurs 14-15 days after the Green Line November peak. In the BOSS data set, the November peak occurs nearly simultaneously in the NaD and Green Line emissions. The second or December peak, occurs approximately 30 days later for NaD and Green Line in both datasets.

A final look at the sodium emission shows that the monthly mean total column of sodium metal model presented in (Marsh et al., 2013), looks to agree with the observed sodium emission (Figure 39, Figure 40). As well, the peak of the airglow emission layer is around 90 km in altitude. Including Figure 41 gives more information. The November and December nightglow peaks occur when the Na layer is near 90km, and the mean total column Na is at a peak as well. The flat region in January corresponds to a period of decreasing layer height, and the February peak occurs during a recovery in Na layer height and a peak in mean total column Na. In addition, the downward trend in the Na nightglow corresponds nicely to the decrease in Na layer height throughout the winter. The addition of temperature trends in the Na layer would add to the analysis and may be made possible by including data from SATI (Sargoytchev et al., 2004) in a future investigation.

A thorough investigation into the latitudinally separated emission phases may reveal temporal patterns in the atmospheric circulation of atomic oxygen and sodium metals near the mesosphere-lower-thermosphere, though this investigation is outside the scope of this thesis.

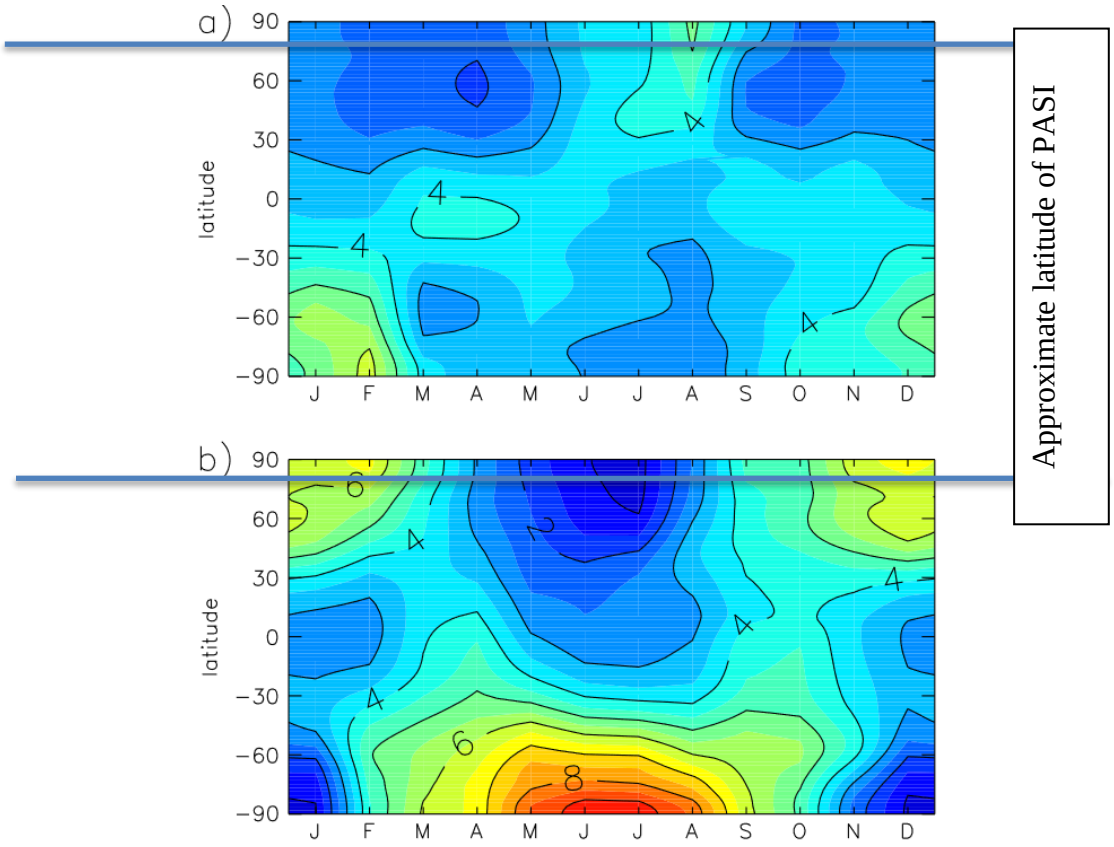

Figure 39: Monthly mean total column (10^9 atom cm^{-2}) of; (a) Na+, (b) Na, adapted from (Marsh et al., 2013). Shown earlier, provided here for convenience.

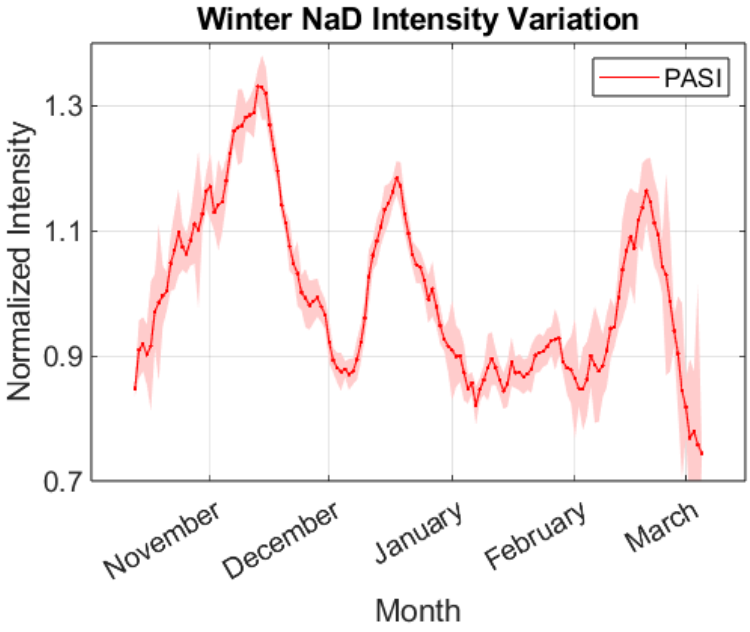

Figure 40 : Winter NaD intensity variation

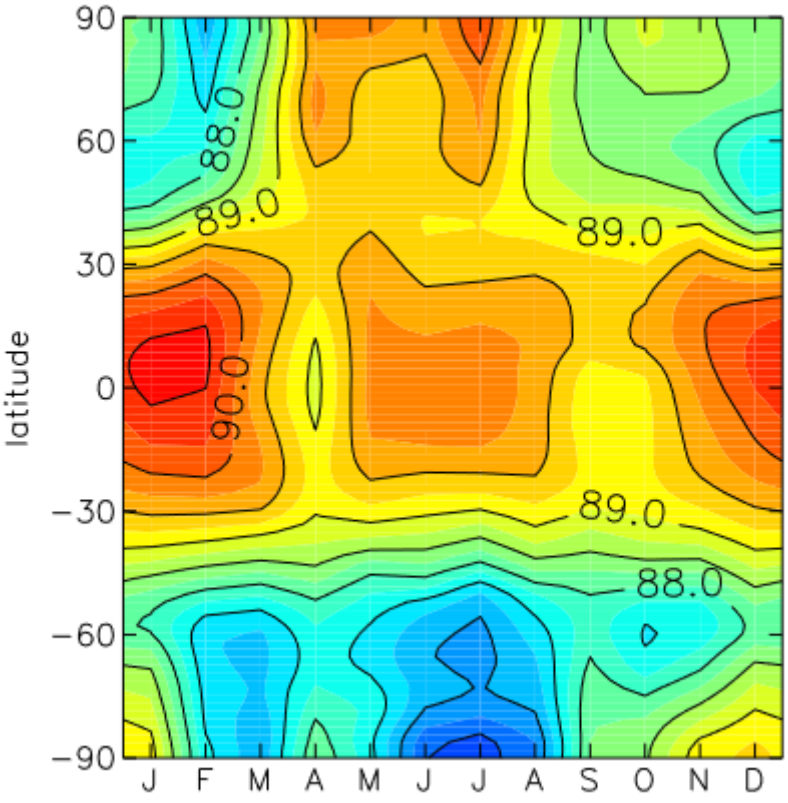

Figure 41: Na layer height (km) (Marsh et al., 2013)

Diurnal Variations

It is well supported in the literature that airglow intensities vary diurnally (Hart, 2019; Ward, 1999). These variations have been attributed to tidal features in the atmosphere, moving the airglow emission layer up and down with the diurnal tides. Further south, these variations are in phase with the tides. However, at high latitudes the effect of the tides is more ambiguous. The question is then what happens at the poles? Is a tide even present at such high latitudes? To explore this question, data from (Hart, 2019) will be used as the low latitude reference. This data originates from coordinates 32.78° N 105.82°W, compared to 80.6N and 86W for PASI data.

Both the BOSS and PASI data used to analyse diurnal trends are binned into 10-minute intervals, and the median of each bin is calculated. Then, the data is smoothed using a 50-minute-wide median filter to minimize outliers. Due to the differences in latitude, the temporal end points in the BOSS data set, and PASI data set will be somewhat different, with PASI data, being further North, extending further from midnight, and the BOSS data set ending approximately 6 hours before/after midnight.

BOSS and PASI both report data with the background continuum removed, reporting only the airglow. Midnight in Eureka varies between 12:30 and 12:58am eastern time (UTC-5), so midnight in these plots of PASI data is at ~0600 UTC. Midnight in Apache Point, New Mexico varies between 11:40pm and 12:10am Mountain Standard

(UTC-7), so midnight in these plots of BOSS data is at ~ 0700 UTC. In both cases midnight is indicated by the blue arrow.

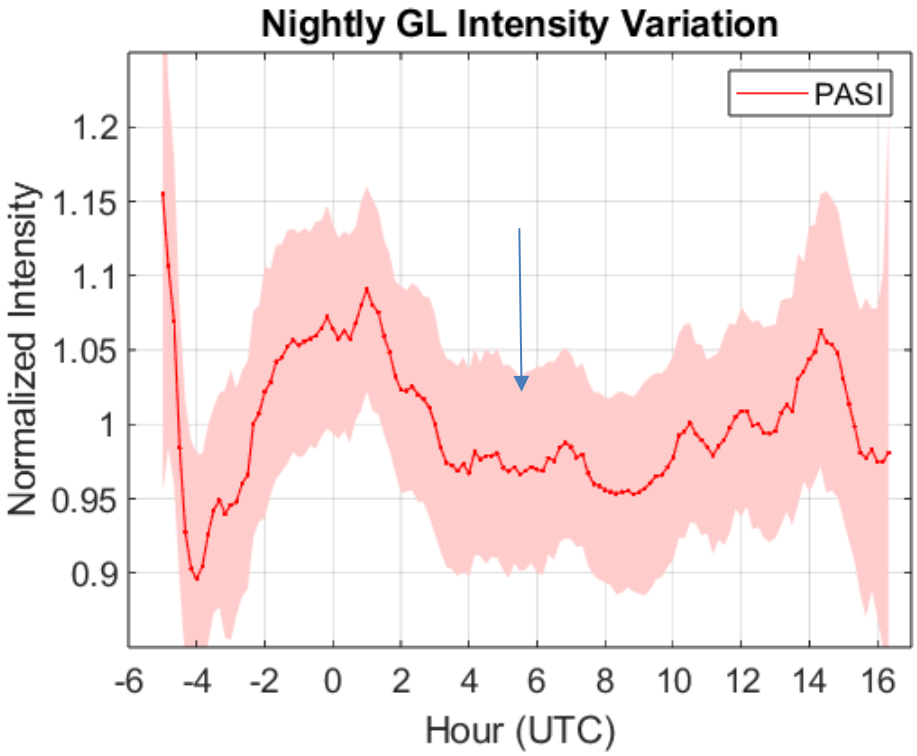

Figure 42: PASI nightly green line (OI) intensity variation with uncertainty represented by the band around the plotted data points.

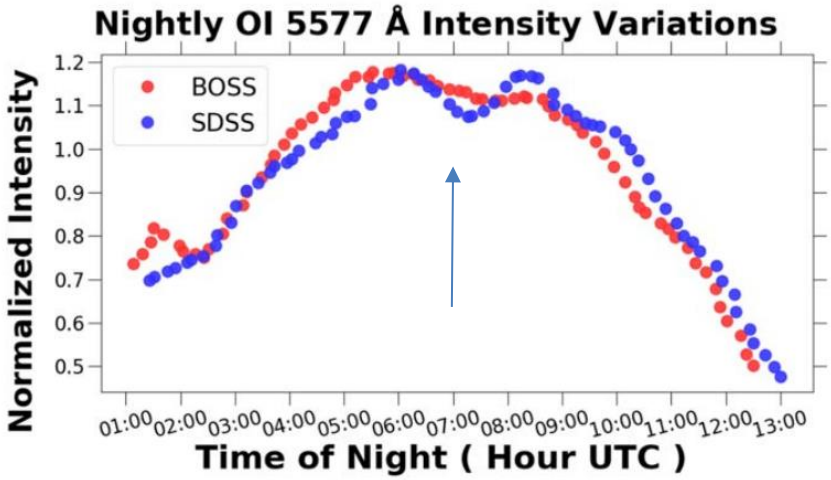

Figure 43: BOSS nightly OI 557.7nm intensity variations (Hart, 2019)

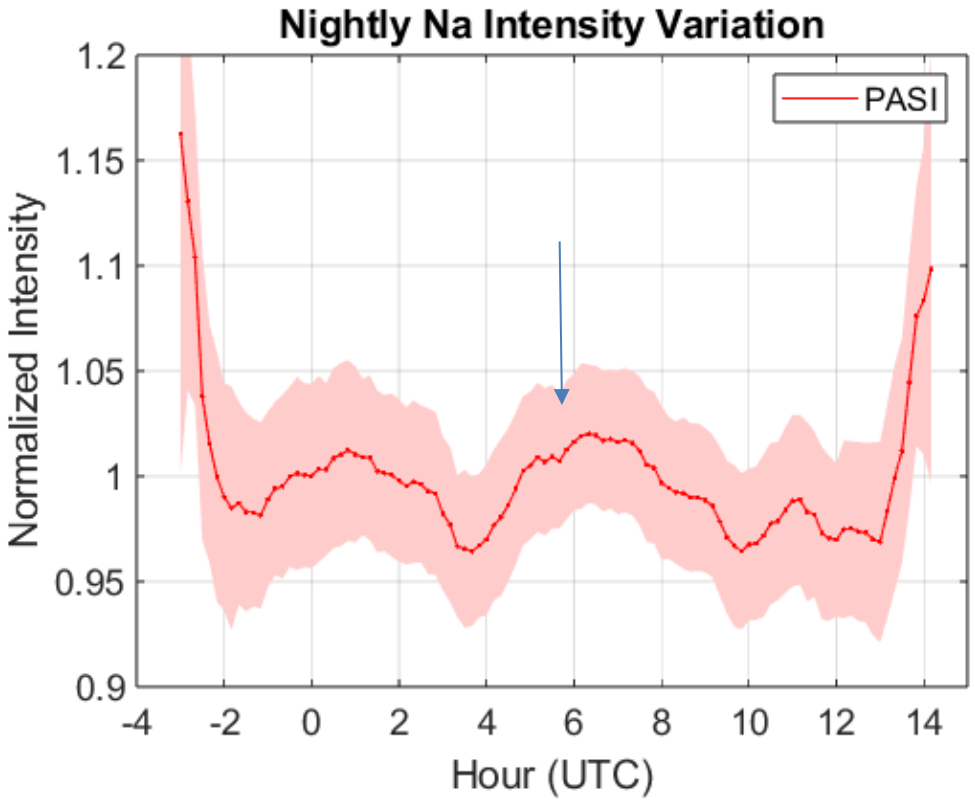

Figure 44: PASI nightly NaD intensity variation with uncertainty represented by the red band

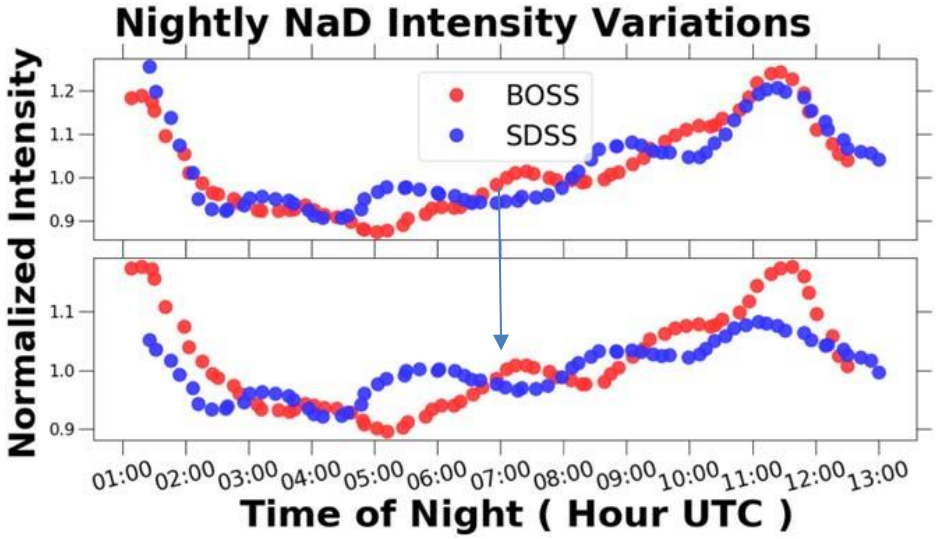

Figure 45: BOSS nightly NaD normalized intensity variations (Hart, 2019)

Atomic oxygen green line shows a clear maximum 6 hours before midnight UTC, relatively flat behaviour for much of the remainder of the night, followed by another increase as the sun approaches twilight. This is somewhat an inverted view of the green emission when compared to the data further south collected by BOSS. The situation is similar with sodium airglow, in that it varies less than the Na emission observed by BOSS further south. Here however, the oscillatory feature is present in both the PASI and BOSS data set, the difference being that the high arctic data does not contain the same upward trend as the mid latitude data. Though not an exact 1:1 comparison, as BOSS includes night glow during the summer months as well as the winter months, there is clear evidence of strong variations in the polar nightglow similar to those further south (Table 8: Nightglow Variations) where there is no concern of a lack of solar radiation to drive photo dissociation. Clearly, atomic oxygen is being transported to the polar regions.

Table 8: Nightglow Variations for nightly, annual, and long-term time scales calculated for PASI and BOSS data by subtracting the minimum value from the maximum value, and dividing by the average of the emission for the corresponding timescale

Emission	$I_{nightly}$ (%)	I_{annual} (%)	I_{long} (%)	Spearman Correlation with SSN (r,p)
OI 557.7nm (PASI)	26	1.45	1.18	(0.96, 0.0002)
NaD 589.3nm (PASI)	20	60	30	(0.90, 0.002)
OI 557.7nm (BOSS)	67	95	39	X
NaD 589.0(589.5) nm (BOSS)	37(28)	112(99)	30(20)	X

Long-term/Solar Cycle Variations

It has been hypothesized that increases in solar output, sunspot number being one marker of this, should coincide with an increase in airglow emissions. The argument being that atomic oxygen is generated through photo-dissociation, thus a greater solar output should increase the presence of atomic oxygen in the atmosphere. The result would be brighter airglow emissions during periods of high solar activity, like solar maximum, and dimmer airglow during periods of low solar activity, like solar minimum. In a high arctic dataset, the situation is complicated. There is minimal sunlight in the high arctic during the winter months, thus any airglow emissions that are present, are due to atomic oxygen that has been produced earlier in the year or has been transported from somewhere else. Despite this, Figure 45 and Figure 49 show the same 2013 emission rate drop, recalling that BOSS is in New Mexico and PASI is in Eureka, Nunavut. This drop corresponds to a drop in solar output at the same time, as seen in Figure 48. It is made clear that this change in airglow output is preceded by a drop in solar output by several months, rather than an instantaneous effect. By shifting the focus to the solar output of only the winter months, this becomes clear as there is a lack of the same dip in the sunspot number. Clearly the airglow is affected, quite strongly in fact, by the solar output months after the sudden drop in sunspot number. Even more striking is the decrease in green line emission rates of approximately 50% from 2012 to 2014. During this same time the sunspot number appears to drop to half.

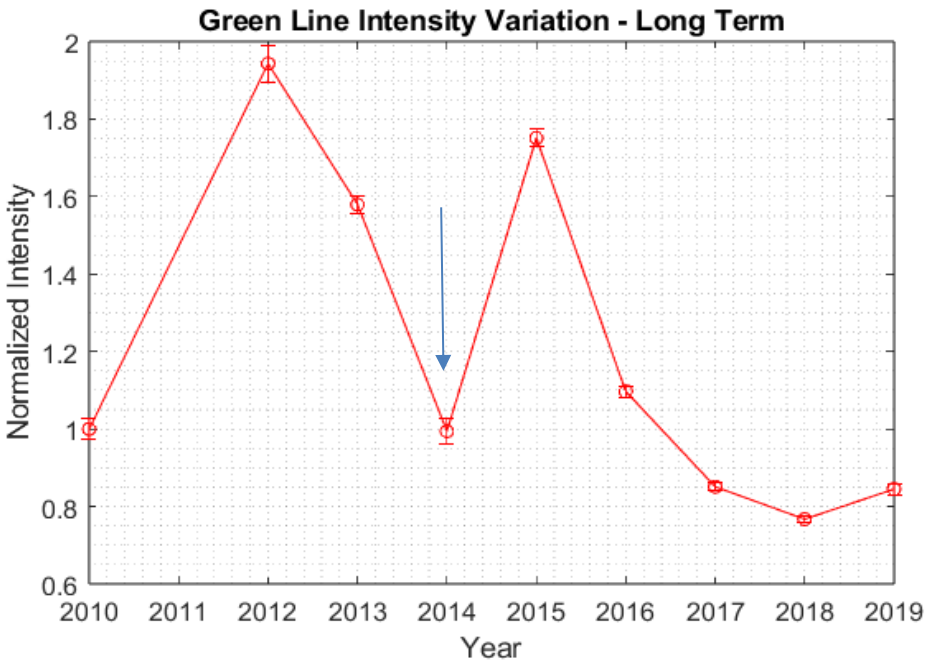

Figure 46: PASI long-term green line winter emission rates, centered on January 1st of each year

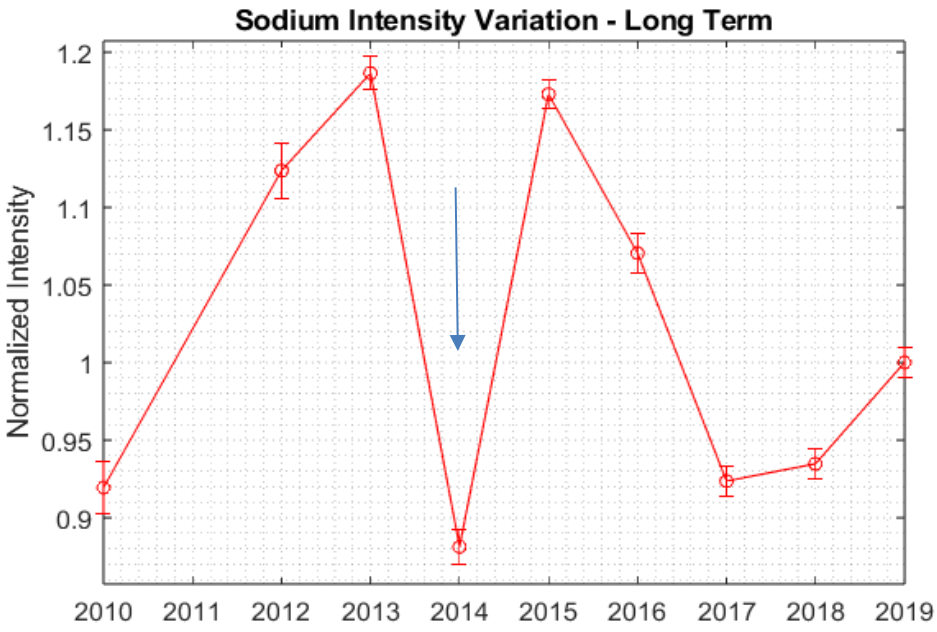

Figure 47: PASI long-term sodium winter emission rates, centered on near January 1st of each year

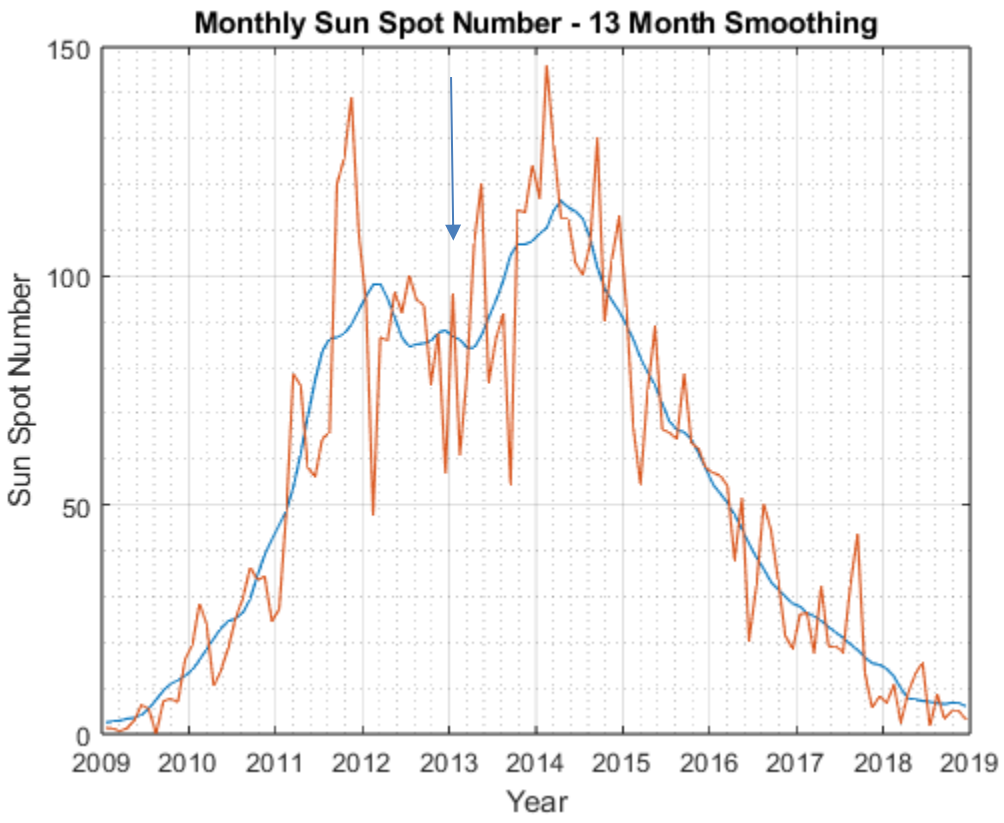

Figure 48: Monthly average sunspot number (SSN) showing drop in 2012-2013 (Source: WDC-SILSO, Royal Observatory of Belgium, Brussels)

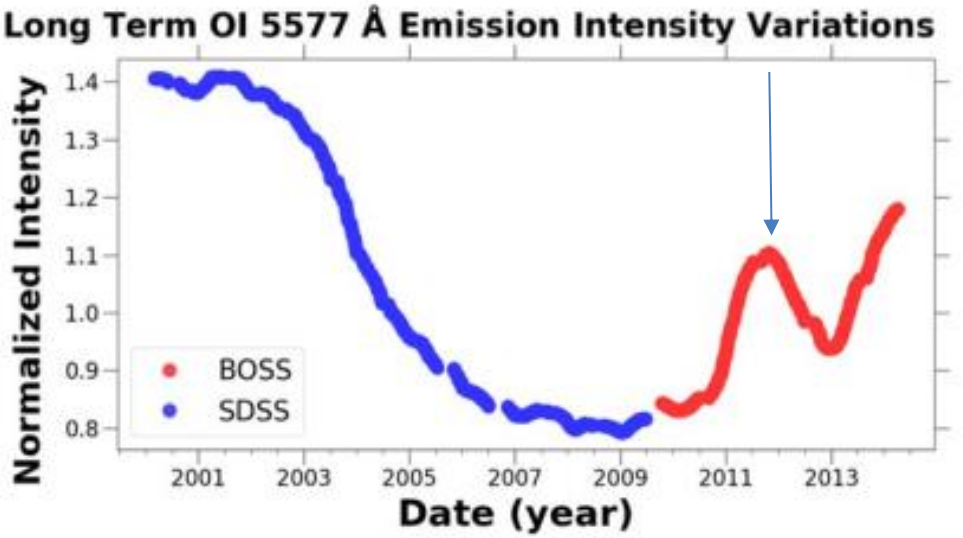

Figure 49: BOSS long-term green line emission rates (Hart, 2019)

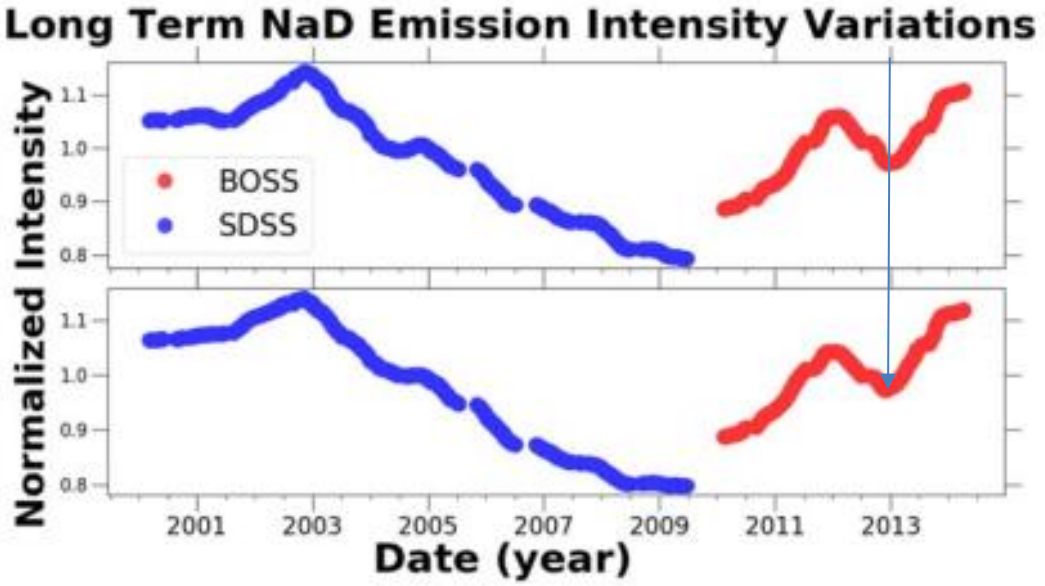

Figure 50: BOSS long-term NaD emission rates (Hart, 2019)

The peak in SSN occurs 25% of the way through 2014, or near the end of March/just after the vernal equinox (Figure 48). This peak shows up in 2015 for both Na and GL and

thus appears anomalous when plotted against the SSN Figure 51. This difference is most likely caused by a delayed response from the nightglow to the SSN. However, in this dataset it is difficult to explore the exact nature of this offset as the PASI data includes only October through March, the winter months, whereas the Sun's influence is continuous. The peak in nightglow caused by the SSN peak in 2014 is likely to affect the airglow more than is evident in the data set due to the sharp drop in SSN after this peak and the nature of averaging. Interestingly, the airglow emission rate falls much more rapidly than the SSN, dropping to levels similar to time periods of much lower SSN, with the green line showing greater variability than the Na. As the atmosphere is a system, this is indicative of feedback loops beyond the simple model of "SSN up equals airglow down", though this does not negate the clear fact that the airglow emission rates are directly affected by solar activity. Clearly, a future experiment would include the summer months as well as the winter months providing continual, yearly observations. This would allow a more accurate determination of the delay present between changes in SSN and observable changes in airglow. Then, it becomes possible to compare these observations with those present in other locations to build a map of sorts of delays in changes to the airglow including day, night, and twilight glow, ultimately resulting in the better understanding of airglow dynamics and subsequently the circulation of earth's atmosphere.

The relationship between nightglow and SSN is better articulated in the following three figures (Figure 51, Figure 52, Figure 53).

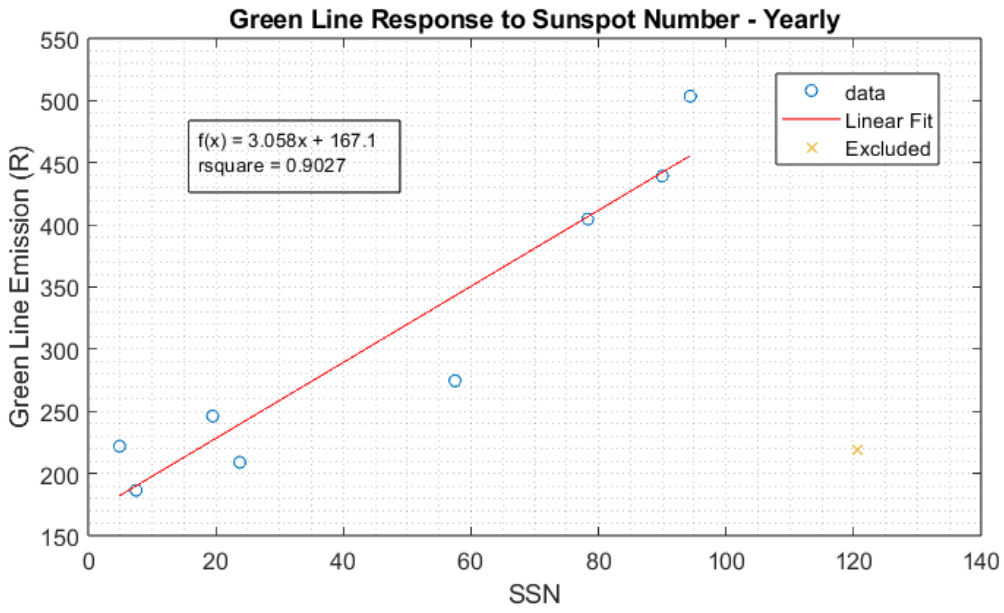

Figure 51: Greenline response to SSN

In both Figure 51 and Figure 52, a single point has been excluded (shown as a yellow “x”). This is the point of highest SSN and corresponds to a large dip in both green, and Na nightglow in the high arctic PASI data. However, this point is also a peak in the more southern BOSS data. This is indicative of a delay between airglow brightness variation and changes in SSN, particularly in nightglow further from the equator and closer to the winter pole. Excluding this point and fitting a linear model to the remaining years shows that both green and sodium nightglow have a linear relationship to SSN (Table 9). When both the nightglow and SSN are plotted normalized one on top of the other (Figure 53) it becomes clear that Na nightglow responds differently than green nightglow to changes in SSN. Perhaps the change is a bit slower, but certainly the change is of a smaller magnitude.

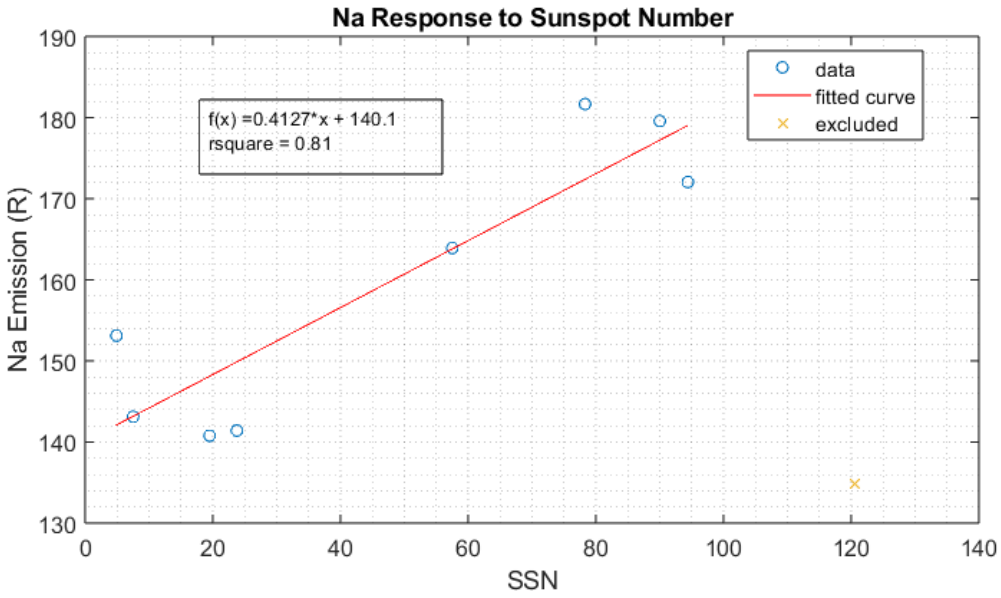

Figure 52: Na response to SSN

Table 9: Nightglow SSN response model fit summary models used, coefficients, and goodness of fit metrics.

	Model	a	b	R^2 (R^2all points)	p-value (all)	RMSE
GREEN (557.7nm)	$I = ax + b$	3 ± 1	167±59	0.9(0.36)	0.007 (0.16)	40.6
Na (589.3nm)	$I = ax + b$	0.4 ±0.2	140 ±12	0.90(0.40)	0.002 (0.29)	8.03

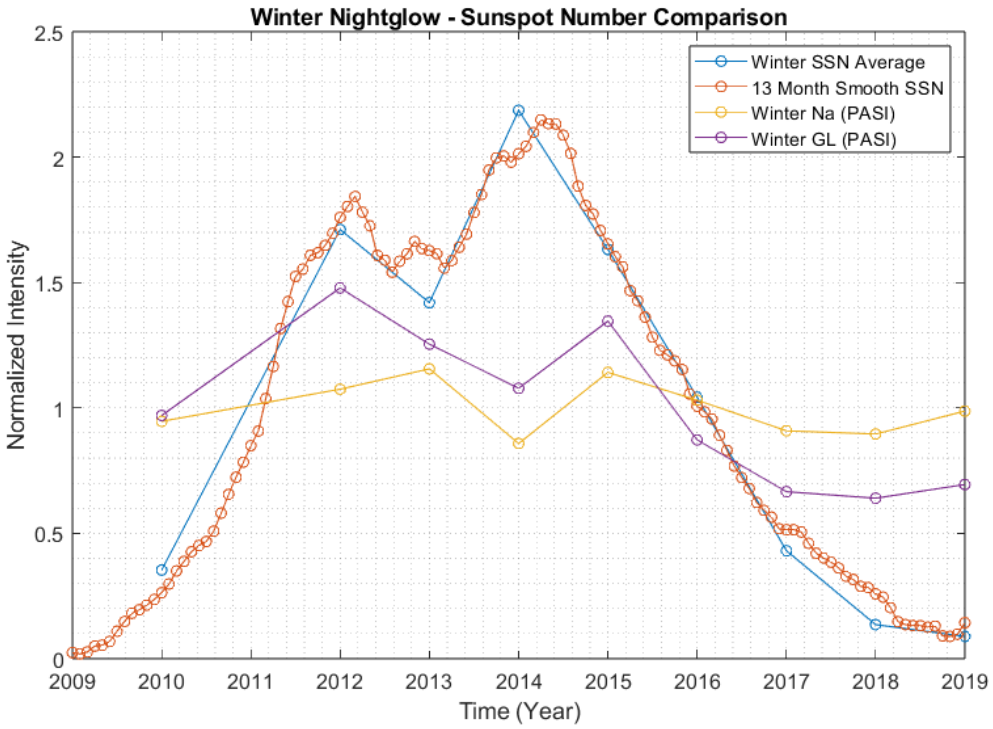

Figure 53: Winter nightglow - SSN comparison

Chapter 4: Conclusion and Future Work

So, what can be concluded from this thesis? First and foremost, there is now a robust data set available from the PASI instrument in the Canadian high arctic. This data set spans nearly a decade of winter observations for the atomic oxygen green (557.7nm) and sodium doublet (NaD 589.3nm) night glow, providing contextual information for co-located instrumentation at the PEARL Observatory in Eureka, Nunavut, like the IR temperature sensor, and the spectral airglow intensity imager (SATI). This data set now available for airglow studies where location-based information, and absolute airglow intensities are of interest.

In this thesis, the raw observations were calibrated and sorted, and the resulting data set used to this data set to study the climatology of airglow emissions as they pertain to nightly, yearly, and long-term timescales. It has been found that while patterns exist in the high-Arctic airglow which are similar to those found further south (Hart, 2019) the magnitudes and phase vary. Perhaps the most interesting conclusion is that during solar cycle 24, a steep decline in sunspot number corresponds to a similarly sharp decline in the green as well as the sodium doublet emissions. As these airglow emissions are predicated on the presence of atomic oxygen in the MLT, it stands to reason that this decrease in emission rate is due to less photodissociation of molecular oxygen from the decrease in solar output. While this emission rate decrease is present in both the high arctic PASI data set and the mid-latitude BOSS data set, the absence of direct solar radiation on the winter

pole, and the delayed response, provides evidence that atomic oxygen transportation is an important factor in the continued generation of airglow at the winter poles.

While this work is concluded, it is useful to consider what further studies may be possible. From here, exploring the same trends in the southern hemisphere as well as on the other side of the globe may improve understanding of the transport of airglow. Though this thesis showed agreement between two different stations with a latitudinal separation, corroborating results with data from other more varied sites, as well as satellite observations, would be prudent. Expanding the scope to include dayglow and the transition between day and night (twilight glow) may reveal something about the rates of transport of important chemical constituents. Expanding on the work related to optical depth alluded to in this thesis and finding a way to estimate aerosol optical depths using an all-sky imager could prove extremely useful for remote measurements, and take advantage of the ability to estimate viewing conditions using the presence/absence of stars as shown in this thesis.

Bibliography

Baibakov, K., N. T. O'Neill, L. Ivanescu, T. J. Duck, C. Perro, A. Herber, K. H. Schulz, and O. Schrems. 2015. "Synchronous Polar Winter Starphotometry and Lidar Measurements at a High Arctic Station." *Atmospheric Measurement Techniques* 8(9):3789–3809. doi: 10.5194/amt-8-3789-2015.

Barbier, Daniel, and F. E. Roach. 1950. "Sodium in the Upper Atmosphere." *Transactions, American Geophysical Union* 31(1):13. doi: 10.1029/TR031i001p00013.

Barth, C. A., and A. F. Hildebrandt. 1961. "The 5577 A Airglow Emission Mechanism." *Journal of Geophysical Research* 66(3):985–86. doi: 10.1029/JZ066i003p00985.

Bodhaine, Barry A., Norman B. Wood, Ellsworth G. Dutton, and James R. Slusser. 1999. "On Rayleigh Optical Depth Calculations." *Journal of Atmospheric and Oceanic Technology* 16(11):1854–61. doi: 10.1175/1520-0426(1999)016<1854:ORODC>2.0.CO;2.

Chapman, S. 1939. "Notes on Atmospheric Sodium." Retrieved October 3, 2022 (https://adsabs.harvard.edu/pdf/1939ApJ....90..309C).

Clemesha, B. R., D. M. Simonich, P. P. Batista, and H. Takahashi. 2005. "Seasonal Variation in the Solar Diurnal Tide and Its Possible Influence on the Atmospheric Sodium Layer." *Advances in Space Research* 35(11):1951–56. doi: 10.1016/j.asr.2005.02.081.

Clemesha, B. R., D. M. Simonich, H. Takahashi, and S. M. L. Melo. 1993. "A Simultaneous Measurement of the Vertical Profiles of Sodium Nightglow and Atomic Sodium Density in the Upper Atmosphere." *Geophysical Research Letters* 20(13):1347–50. doi: 10.1029/93GL01121.

Das, Uma, C. J. Pan, and H. S. S. Sinha. 2011. "Effects of Solar Cycle Variations on Oxygen Green Line Emission Rate over Kiso, Japan." *Earth, Planets and Space* 63(8):941–48. doi: 10.5047/eps.2011.04.006.

Elvey, C. T. 1950. "Progress in Studies of the Airglow in Upper Air Research." *American Journal of Physics* 18(7):431–37. doi: 10.1119/1.1932627.

Fukuyama, K. 1977. "Airglow Variations and Dynamics in the Lower Thermosphere and Upper Mesosphere—II. Seasonal and Long-Term Variations." *Journal of Atmospheric and Terrestrial Physics* 39(1):1–14. doi: 10.1016/0021-9169(77)90038-1.

Hart, Murdock. 2019. “Long-Term Spectroscopic Observations of the Atmospheric Airglow by the Sloan Digital Sky Survey.” *Publications of the Astronomical Society of the Pacific* 131(995):015003. doi: 10.1088/1538-3873/aae972.

Huang, Tai-Yin. 2018. “Influences of CO2 Increase, Solar Cycle Variation, and Geomagnetic Activity on Airglow from 1960 to 2015.” *Journal of Atmospheric and Solar-Terrestrial Physics* 171:164–75. doi: 10.1016/j.jastp.2017.06.008.

Kaplan, Joseph. 1931. “The Light of the Night Sky.” *Physical Review* 38(5):1048–51. doi: 10.1103/PhysRev.38.1048.

Marsh, Daniel R., Diego Janches, Wuhu Feng, and John M. C. Plane. 2013. “A Global Model of Meteoric Sodium.” *Journal of Geophysical Research: Atmospheres* 118(19):11,442-11,452. doi: 10.1002/jgrd.50870.

Mcdade, I. C., E. J. Llewellyn, R. G. H. Greer, and D. P. Murtagh. 1986. “ETON 3: Altitude Profiles of the Nightglow Continuum at Green and near Infrared Wavelengths.” *Planetary and Space Science* 34(9):801–10. doi: 10.1016/0032-0633(86)90076-0.

McDade, I. C., D. P. Murtagh, R. G. H. Greer, P. H. G. Dickinson, G. Witt, J. Stegman, E. J. Llewellyn, L. Thomas, and D. B. Jenkins. 1986. “ETON 2: Quenching Parameters for the Proposed Precursors of O2(b1Σg+) and O(1S) in the Terrestrial Nightglow.” *Planetary and Space Science* 34(9):789–800. doi: 10.1016/0032-0633(86)90075-9.

McGill, Robert, John W. Tukey, and Wayne A. Larsen. 1978. “Variations of Box Plots.” *The American Statistician* 32(1):12. doi: 10.2307/2683468.

McLennan, John Cunningham. 1928. “Bakerian Lecture.—The Aurora and Its Spectrum.” *Proceedings of the Royal Society of London. Series A, Containing Papers of a Mathematical and Physical Character* 120(785):327–57. doi: 10.1098/rspa.1928.0153.

Murray, Kevin. 2013. “Atmosphere.” Retrieved August 20, 2022 (https://www.thinglink.com/scene/343846388821393409).

Murtagh, D. P., G. Wii-I, J. Stegman, C. McDADE, and E. J. Llewellyn. 1989. “AN ASSESSMENT OF PROPOSED 0(‘S) AND O,(b’ZC,+) NIGHTGLOW EXCITATION PARAMETERS.” 11.

O’Neill, Norman T., Konstantin Baibakov, Sareh Hesaraki, Liviu Ivanescu, Randall V. Martin, Chris Perro, Jai P. Chaubey, Andreas Herber, and Thomas J. Duck. 2016. “Temporal and Spectral Cloud Screening of Polar Winter Aerosol Optical Depth(AOD): Impact of Homogeneous and Inhomogeneous Clouds and Crystal Layers Onclimatological-Scale AODs.” *Atmospheric Chemistry and Physics* 16(19):12753–65. doi: 10.5194/acp-16-12753-2016.

Perezramirez, D., J. Aceituno, B. Ruiz, F. Olmo, and L. Aladosarboledas. 2008. "Development and Calibration of a Star Photometer to Measure the Aerosol Optical Depth: Smoke Observations at a High Mountain Site." *Atmospheric Environment* 42(11):2733–38. doi: 10.1016/j.atmosenv.2007.06.009.

Plane, John M. C. 1991. "The Chemistry of Meteoric Metals in the Earth's Upper Atmosphere." *International Reviews in Physical Chemistry* 10(1):55–106. doi: 10.1080/01442359109353254.

Plane, John M. C. 2003. "Atmospheric Chemistry of Meteoric Metals." *Chemical Reviews* 103(12):4963–84. doi: 10.1021/cr0205309.

Plane, John, Hilke Oetjen, Marcelo de Miranda, Alfonso Saiz-Lopez, Michael Gausa, and Bifford Williams. 2012. "On the Sodium D Line Emission in the Terrestrial Nightglow." *Journal of Atmospheric and Solar-Terrestrial Physics* 74:181–88. doi: 10.1016/j.jastp.2011.10.019.

Rayleigh, Lord. 1921. "The Aurora Line in the Spectrum of the Night Sky." 13.

Roach, F. E., and A. B. Meinel. 1955. "The Height of the Nightglow by the Van Rhijn Method." *The Astrophysical Journal* 122:530. doi: 10.1086/146115.

Rosenberg, N., and S. P. Zimmerman. 1966. "CORRELATION BETWEEN THE 5577 A [01] NIGHT AIRGLOW INTENSITY AND SOLAR ACTIVITY." 10.

Russel, Henry. 1917. "The Permanent Aurora." *SCIENTIFIC AMERICAN* 2.

Russell, Jason P., W. E. Ward, R. P. Lowe, R. G. Roble, G. G. Shepherd, and B. Solheim. 2005. "Atomic Oxygen Profiles (80 to 115 Km) Derived from Wind Imaging Interferometer/Upper Atmospheric Research Satellite Measurements of the Hydroxyl and Greenline Airglow: Local Time–Latitude Dependence." *Journal of Geophysical Research: Atmospheres* 110(D15). doi: 10.1029/2004JD005570.

Sargoytchev, Stoyan I., Stephen Brown, Brian H. Solheim, Young-Min Cho, Gordon G. Shepherd, and Maria Jose López-González. 2004. "Spectral Airglow Temperature Imager (SATI): A Ground-Based Instrument for the Monitoring of Mesosphere Temperature." *Applied Optics* 43(30):5712. doi: 10.1364/AO.43.005712.

Silverman, S. M. 1970. "Night Airglow Phenomenology." *Space Science Reviews* 11(2–3). doi: 10.1007/BF00241526.

Slanger, T. G., P. C. Cosby, D. L. Huestis, A. Saiz-Lopez, B. J. Murray, D. A. O'Sullivan, J. M. C. Plane, C. Allende Prieto, F. J. Martin-Torres, and P. Jenniskens. 2005. "Variability of the Mesospheric Nightglow Sodium D2/D1 Ratio." *Journal of Geophysical Research: Atmospheres* 110(D23). doi: 10.1029/2005JD006078.

Smee, Stephen A., James E. Gunn, Alan Uomoto, Natalie Roe, David Schlegel, Constance M. Rockosi, Michael A. Carr, French Leger, Kyle S. Dawson, Matthew D. Olmstead, Jon Brinkmann, Russell Owen, Robert H. Barkhouser, Klaus Honscheid, Paul Harding, Dan Long, Robert H. Lupton, Craig Loomis, Lauren Anderson, James Annis, Mariangela Bernardi, Vaishali Bhardwaj, Dmitry Bizyaev, Adam S. Bolton, Howard Brewington, John W. Briggs, Scott Burles, James G. Burns, Francisco Javier Castander, Andrew Connolly, James R. A. Davenport, Garrett Ebelke, Harland Epps, Paul D. Feldman, Scott D. Friedman, Joshua Frieman, Timothy Heckman, Charles L. Hull, Gillian R. Knapp, David M. Lawrence, Jon Loveday, Edward J. Mannery, Elena Malanushenko, Viktor Malanushenko, Aronne James Merrelli, Demitri Muna, Peter R. Newman, Robert C. Nichol, Daniel Oravetz, Kaike Pan, Adrian C. Pope, Paul G. Ricketts, Alaina Shelden, Dale Sandford, Walter Siegmund, Audrey Simmons, D. Shane Smith, Stephanie Snedden, Donald P. Schneider, Mark SubbaRao, Christy Tremonti, Patrick Waddell, and Donald G. York. 2013. "THE MULTI-OBJECT, FIBER-FED SPECTROGRAPHS FOR THE SLOAN DIGITAL SKY SURVEY AND THE BARYON OSCILLATION SPECTROSCOPIC SURVEY." *The Astronomical Journal* 146(2):32. doi: 10.1088/0004-6256/146/2/32.

Veselinovic, Dragan. 2011. "Atmospheric Gravity Waves Detected in the Arctic Atmosphere by an All Sky Airglow Imager." Library and Archives Canada = Bibliotheque et Archives Canada, Ottawa.

Ward, W. E. 1999. "A Simple Model of Diurnal Variations in the Mesospheric Oxygen Nightglow." *Geophysical Research Letters* 26(23):3565–68. doi: 10.1029/1999GL003661.

Ward, William, Annika Seppälä, Erdal Yiğit, Takuji Nakamura, Claudia Stolle, Jan Laštovička, Thomas N. Woods, Yoshihiro Tomikawa, Franz-Josef Lübken, Stanley C. Solomon, Daniel R. Marsh, Bernd Funke, and Duggirala Pallamraju. 2021. "Role Of the Sun and the Middle Atmosphere/Thermosphere/Ionosphere In Climate (ROSMIC): A Retrospective and Prospective View." *Progress in Earth and Planetary Science* 8(1):47. doi: 10.1186/s40645-021-00433-8.

Weaver, Dan. 2016. "CREATE Arctic Science: Image." Retrieved January 5, 2023 (https://createarcticscience.files.wordpress.com/2016/03/figure-3-eu-yk-to_2016_sunlight.png).

Zotti, Georg, Susanne M. Hoffmann, Alexander Wolf, Fabien Chéreau, and Guillaume Chéreau. 2021. "Simulated Sky: Stellarium for Cultural Astronomy Research." *Journal of Skyscape Archaeology* 6(2). doi: 10.1558/jsa.17822.

Zubov, V., E. Rozanov, T. Egorova, I. Karol, and W. Schmutz. 2013. "Role of External Factors in the Evolution of the Ozone Layer and Stratospheric Circulation in 21st Century." *Atmospheric Chemistry and Physics* 13(9):4697–4706. doi: 10.5194/acp-13-4697-2013.

Zwick, H. H., and G. G. Shepherd. 1963. “RATIO AND ABSOLUTE BRIGHTNESS MEASUREMENTS OF THE SODIUM *D* LINES IN THE TWILIGHT GLOW.” *Canadian Journal of Physics* 41(2):343–54. doi: 10.1139/p63-037.

Curriculum Vitae

Candidate's full name: Dustin Glen Gamblin

Universities attended: University of New Brunswick

BSc Physics, 2017

Publications:

1. "Identifying Gravity Waves with Periods Greater than Two Hours Using an All-Sky Airglow Imager Located in Eureka, Nunavut." (2017). Bachelor's, University of New Brunswick, Fredericton, Canada, April 2017.

Conference Presentations:

1. "Long-term trends in optical airglow observations in the Canadian high arctic." 9th Vertical Coupling of the Atmosphere-Ionosphere System (VCAIS) and 6th Antarctic Gravity Wave Instrument Network (ANWGIN) workshop, Fredericton, New Brunswick, Canada, June 2024.
2. "Polar airglow trends derived from the PEARL All-Sky Imager (PASI) observations in Eureka, Nunavut." Canadian Meteorological and Oceanographic Society (CMOS), Online, June 2020.
3. "PASI: Qualifying Nightglow Data and Preliminary Trends." Canadian Network for the Detection of Atmospheric Change (CANDAC) Workshop, Online, Summer 2020.
4. "The Importance and Restoration of Urban Waterways." Canadian Parks and Wilderness Society (CPAWS) Stewardship Program Summit, Ottawa, Ontario, Canada, February 2020.

5. “Airglow Climatology in the Canadian High Arctic.” “International Union of Geodesy and Geophysics” (IUGG), Montreal, Quebec, Canada, July 2019.
6. “The Brightness of the Sky and the PEARL All-Sky Imager.” Division of Atmospheric and Space Physics (DASP) Saskatoon, Saskatchewan, Canada, 2019.
7. “Characterizing Airglow Emissions as a Function of Solar Zenith Angle.” the Scientific Committee on Solar-Terrestrial Physics (SCOSTEP), Toronto, Ontario, Canada, July 2018.
8. “The Characterization of the PEARL All-Sky Imager.” Probing the Atmosphere of the High Arctic (PAHA) Toronto, Ontario, Canada, June 2018.
9. “Characterizing Gravity Waves using PASI and SATI at PEARL in Eureka, Nunavut.” Canadian Meteorological and Oceanographic Society (CMOS), Halifax, Nova Scotia, Canada, June 2018.
10. “Airglow Observations with the PEARL All-Sky Imager.” Arctic Net Arctic Change, Quebec City, Quebec, Canada, December 2017.
11. “Detecting Longer Period Gravity Waves through Airglow Emissions over Eureka.” Atlantic Undergraduate Physics and Astronomy Conference (AUPAC) Charlottetown, PEI, Canada, February 2017.
12. “Gravity Waves over Eureka, Nunavut and the PEARL All Sky Imager.” Canadian Undergraduate Physics Conference (CUPC), Halifax, Nova Scotia, Canada, November 2016.